

AD-A178 367

INTENTION PAGE

1a. REPORT SECURITY CLASSIFICATION  
UNCLASSIFIED

b. RESTRICTIVE MARKINGS

2a. SECURITY CLASSIFICATION AUTHORITY

3. DISTRIBUTION/AVAILABILITY OF REPORT

2b. DECLASSIFICATION/DOWNGRADING SCHEDULE

UNLIMITED

4. PERFORMING ORGANIZATION REPORT NUMBER(S)

THC-02GH87021A

5. MONITORING ORGANIZATION REPORT NUMBER(S)

6a. NAME OF PERFORMING ORGANIZATION

The Hokenson Company

6b. OFFICE SYMBOL  
(if applicable)

7a. NAME OF MONITORING ORGANIZATION

U.S. Army Strategic Defense Command

6c. ADDRESS (City, State, and ZIP Code)

840 S. Tremaine Ave.  
Los Angeles, CA 90005

7b. ADDRESS (City, State, and ZIP Code)

P.S. Box 1500  
Huntsville, AL 35807

8a. NAME OF FUNDING/SPONSORING ORGANIZATION

8b. OFFICE SYMBOL  
(if applicable)

9. PROCUREMENT INSTRUMENT IDENTIFICATION NUMBER

DASG60-86-C-0082

8c. ADDRESS (City, State, and ZIP Code)

10. SOURCE OF FUNDING NUMBERS

PROGRAM  
ELEMENT NO.PROJECT  
NO.TASK  
NO.WORK UNIT  
ACCESSION NO.

11. TITLE (Include Security Classification)

Optimal Aerodynamic Shapes for Hypervelocity Projectiles

MAR 25 1987

12. PERSONAL AUTHOR(S)

Dr. Gustave J. Hokenson

13a. TYPE OF REPORT  
Final

13b. TIME COVERED

FROM 86 Jul 31 to 87 Jan 31

14. DATE OF REPORT (Year, Month, Day)

87FEB28

15. PAGE COUNT

59

16. SUPPLEMENTARY NOTATION

17. COSATI CODES

FIELD	GROUP	SUB-GROUP
1	1	

18. SUBJECT TERMS (Continue on reverse if necessary and identify by block number)

Aerodynamics, Hypersonics

19. ABSTRACT (Continue on reverse if necessary and identify by block number)

The feasibility of determining optimal aerodynamic shapes for hypervelocity vehicles by considering, simultaneously, the effects of drag, internal volume distribution and impact effectiveness was investigated by utilizing numerical simulations. Optimal shapes indicated from inviscid considerations were corrected by utilizing state-of-the-art turbulent boundary layer theory. A representative penetrator of maximum size which would fit within the resultant volume distribution was then flown to a typical target and allowed to impact. The loss in kinetic energy of the penetrator along the trajectory was calculated from simple rigid body dynamics and the previously computed projectile total  $C_D$ . The initial stages of impact may then be simulated from a Navier-Stokes analysis with the appropriate metallic physical properties. As a result various candidate optimal shapes may be compared from an overall mission standpoint.

20. DISTRIBUTION AVAILABILITY OF ABSTRACT

 UNCLASSIFIED/UNLIMITED  SAME AS RPT  DTIC USERS

21. ABSTRACT SECURITY CLASSIFICATION

UNCLASSIFIED

22a. NAME OF RESPONSIBLE INDIVIDUAL  
Mr. Lee Webster22b. TELEPHONE (Include Area Code)  
205-895-481822c. OFFICE SYMBOL  
DASD-H-V

DTIC FILE COPY

THE HOKENSON COMPANY

FINAL REPORT

PHASE I SBIR

CONTRACT NO. DASG60-86-C-0082

Optimal Aerodynamic Shapes for Hypervelocity Projectiles

SPONSORED BY:

U.S. ARMY STRATEGIC DEFENSE COMMAND

FEBRUARY 1987

This document has been approved  
for public release and sale; its  
distribution is unlimited.

87 3 25 00



## Executive Summary

↓  
The research objective for Phase I of this work was to demonstrate the feasibility of establishing optimal shapes for hypervelocity projectiles, considering simultaneously the effects of drag, internal volume distribution and impact effectiveness. Utilizing classical optimization analysis and hypersonic inviscid flow theory, minimum pressure drag bodies were obtained subject to various constraints. It was then assumed that the shapes so obtained corresponded to the solid body plus a viscous displacement. Utilizing state-of-the-art turbulent boundary layer theory in an iterative mode, the solid body shape was then determined along with the skin friction drag. Relative to any specified reference penetrator shape, the internal volume distribution effectiveness may then be characterized. Subsequently, the loss in kinetic energy of the projectile along its trajectory is computed and the initial stage of impact is computed from a Navier-Stokes numerical simulation in order to quantify the target damage. As a result of this procedure, various candidate hypervelocity projectile shapes may be competed against one another from an overall mission point of view.

↑

## Discussion

The prediction of optimum aerodynamic shapes has a heritage dating from Newton to the present time. Traditionally, simplified inviscid flow models are combined with classical optimization theory in order to derive minimum drag configurations<sup>1</sup>. More recently, incorporation of viscous effects at on- and off-design conditions has been approached, as shown in the Appendix. Relative to the smart hypervelocity projectile design problem, additional considerations beyond aerodynamic drag are relevant. Included in these are the internal volume distribution and the impact mechanics of the penetrator which fits within that volume. The present research sought to make a contribution to the design of optimally-shaped hypervelocity projectiles by considering all aspects of the mission, including viscous effects on the minimum drag body, as shown in Fig. 1.

Initially, the minimum pressure drag shape (herein assumed to correspond to the solid body plus its viscous displacement) for various constraints may be sought from standard optimization techniques applied to the integral:

$$D = \int C_p d\bar{A}$$

where  $C_p$  is the local pressure coefficient and  $d\bar{A}$  is the local surface area in the stream-wise (drag) direction divided by the base area. According to the Euler-Lagrange equation, the pressure drag is minimized when:

$$d/dx (\partial J/\partial r') - \partial J/\partial r = 0 \quad ,$$

where:

$$J \equiv C_p \, d\tilde{A}/dx$$

$$d\tilde{A}/dx = \tilde{r} \, \tilde{r}'$$

$$\tilde{r} \equiv r/r_{\text{base}}$$

$$\tilde{r}' = d\tilde{r}/dx$$

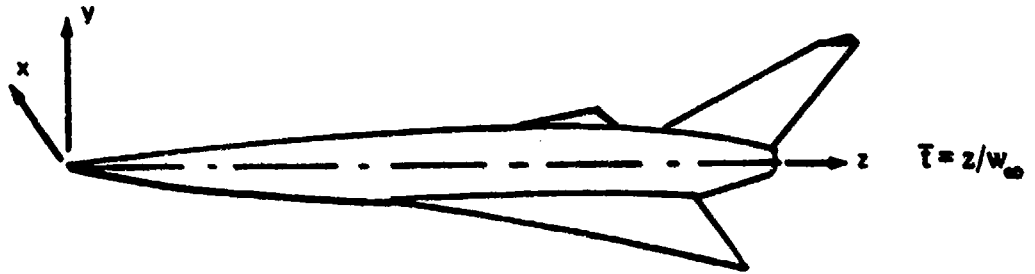
For axisymmetric flow, the Newton-Busemann approximation for the local pressure in hypersonic flow may be written:

$$C_p = 2.0 (\theta^2 + r\theta'/2)$$

where  $\theta$  is the local inclination of the surface to the flow. This simple formula allows the Euler - Lagrange equation to be integrated subject to various constraints, as we shall see. In addition, however, it is possible to integrate the Euler - Lagrange equation numerically and compute the local pressure field from hypersonic small disturbance theory, wherein the streamwise variable becomes 'time-like' and we are able to compute the inviscid field from the equations presented here. This approach readily admits the treatment of non-axisymmetric, for example square cross-section, bodies.

# THE HOKENSON COMPANY

## HYPERSONIC SMALL DISTURBANCE EQUATIONS



$$\frac{\partial \bar{p}}{\partial \xi} + \frac{\partial(\bar{p}u)}{\partial x} + \frac{\partial(\bar{p}v)}{\partial y} = 0$$

$$\frac{\partial \bar{v}}{\partial \xi} + \frac{u}{\beta} \frac{\partial \bar{v}}{\partial x} + \frac{v}{\beta} \frac{\partial \bar{v}}{\partial y} + \frac{1}{\beta} \frac{\partial \bar{p}}{\partial y} = 0$$

$$\frac{\partial \bar{u}}{\partial \xi} + \frac{u}{\beta} \frac{\partial \bar{u}}{\partial x} + \frac{v}{\beta} \frac{\partial \bar{u}}{\partial y} + \frac{1}{\beta} \frac{\partial \bar{p}}{\partial x} = 0$$

$$\frac{\partial}{\partial \xi} (\bar{p}/\beta^\gamma) + \frac{u}{\beta} \frac{\partial}{\partial x} (\bar{p}/\beta^\gamma) + \frac{v}{\beta} \frac{\partial}{\partial y} (\bar{p}/\beta^\gamma) = 0$$

$$\frac{\partial n}{\partial \xi} + \bar{u} n_x + \bar{v} n_y = 0$$

$$y, x \rightarrow \infty, \quad \bar{v}, \bar{u} \rightarrow 0, \quad \bar{p} \rightarrow \bar{p}_\infty, \quad \beta \rightarrow \beta_\infty$$

Various shapes which result from the Newton-Busemann formula shall be discussed in the next section.

As mentioned earlier, for the purposes of this research, the shapes so derived were assumed to be associated with the solid body plus its viscous displacement. The validity of the assumption in hypersonic flow rests on the fact that the displacement thickness,  $\delta^*$ , approximately equals the boundary layer thickness,  $\delta$ , and, from considerations of continuity, the slope of the inviscid streamlines at the edge of the boundary layer equals the streamwise gradient of the displacement thickness:

$$\tan \theta_e = V_e / U_e = d\delta^*/dx$$

Therefore, in hypersonic flow, the edge of the boundary layer is approximately an inviscid flow streamline. It is well known that, in inviscid flow, any streamline may be replaced by a solid boundary. As a result, the solid body shapes which support the computed optimum viscous displacement shapes may be obtained simply by subtracting  $\delta^*$ .

Several caveats apply here, however. First, if the flowfield conditions do not justify the approximation that  $\delta^* \rightarrow \delta$ , the  $\delta^*$  correction procedure must be modified. In addition, we note that in hypersonic flow this approach is not equivalent to the heuristic use of  $\delta^*$  corrections in, for example, internal flows where the equivalent uniform inviscid flow is often introduced on the basis of global conservation of mass flow arguments. Finally, the definition of  $\delta^*$  for slender bodies must be treated with some care as explained in the following article.

Reprinted from AIAA JOURNAL, Vol. 15, No. 4, April 1977, pp. 597-600  
Copyright, 1977, by the American Institute of Aeronautics and Astronautics, and reprinted by permission of the copyright owner

## Consistent Integral Thickness Utilization for Boundary Layers with Transverse Curvature

G.J. Hokenson\*

*STD Research Corporation, Arcadia, Calif.*

### Nomenclature

- $A$  = area  
 $a$  = coefficient in Eqs. (16),  $\bar{T}_s$   
 $b$  = coefficient in Eqs. (16),  $(\bar{T}_{sw} - \bar{T}_s) \epsilon$   
 $c$  = coefficient in Eqs. (16),  $1.0 - \bar{T}_{sw}$   
 $C_f$  = skin friction coefficient

Received Sept. 16, 1976; revision received Dec. 16, 1976.  
Index category: Boundary Layers and Convective Heat Transfer -  
Turbulent.

\*Senior Scientist and Group Manager, Physical Sciences. Member  
AIAA.

**D** = local body diameter  
**H** = shape factor,  $\delta^*/\theta$   
**h** = enthalpy  
**M** = Mach number  
**N** = exponent in power law property profiles  
**Pr** = Prandtl number  
**R** = local body radius  
**Re** = Reynolds number  
**T** = temperature  
**u** = streamwise velocity component  
**W** = two-dimensional width, Eq. (3)  
**x** = streamwise coordinate  
**y** = coordinate normal to body surface  
 **$\alpha$**  = local slope of body surface, Eq. (7)  
 **$\gamma$**  = ratio of specific heats  
 **$\delta$**  = boundary-layer thickness  
 **$\delta^*$**  = displacement thickness, Eq. (1)  
 **$\delta_h$**  = enthalpy thickness  
 **$\epsilon$**  = function of Prandtl number and flowfield parameters  
 **$\rho$**  = density  
 **$\theta$**  = momentum thickness, Eq. (2)  
 **$\tau$**  = transverse curvature parameter, Eq. (10)  
 **$\eta$**  = normalized  $y$  coordinate,  $y/\delta$   
**—** = indicates quantities nondimensionalized by  $\delta$  for integral thicknesses and by freestream values for dependent variables

#### Subscripts

**aw** = adiabatic wall conditions  
 **$\infty$**  = freestream conditions  
 **$o$**  = integral parameters in the form of Eqs. (11) and (12)  
**2D** = two dimensional  
**w** = wall conditions

**B**OUNDARY-layer displacement and momentum thicknesses may be introduced by conceptually uniformizing the flowfield properties throughout the boundary layer. In order that the mass flux past the wall in the streamwise direction equal that in the boundary layer with nonuniform flow, the wall (and therefore the external flow streamlines) must be shifted a distance  $\delta^*$  normal to its own plane. Expressed in mathematical terms, this can be written

$$\int_0^{\delta^*} \rho_w u_w dA = \int_0^{\delta} \rho_w u_w dA \quad (1)$$

Similarly, the net momentum defect of the nonuniform flow in the boundary layer must be matched by the uniformized flow, forcing the total momentum in a layer of thickness  $\theta$  adjacent to the wall to be accounted for through the relationship

$$\int_0^{\theta} \rho_w u_w^2 dA = \int_0^{\delta} \rho_w u_w (u_w - u) dA \quad (2)$$

In both Eqs. (1) and (2) a coordinate system which is attached to the wall has been utilized and the  $y$ -axis is assumed to be normal to the local body surface. In the two-dimensional configuration, the differential area through the boundary layer is

$$dA = W dy \quad (3)$$

where  $W$  is the local transverse flowfield dimension. With this expression applied to Eqs. (1) and (2), the following classical formulas can be derived

$$\delta_{2D}^* = \int_0^1 (1 - \beta u) d\eta \quad (4)$$

and

$$\theta_{2D} = \int_0^1 \beta u (1 - u) d\eta \quad (5)$$

The terms on the right hand side of Eqs. (4) and (5) are also the exact form of the grouping of variables which appear in the two-dimensional integral boundary-layer equations.

For the axisymmetric situation, the local differential area through the boundary layer may be written

$$dA = 2\pi(R \pm y \cos \alpha) dy \quad (6)$$

where:

$$\alpha = \tan^{-1}(dR/dx) \quad (7)$$

The + or - sign in Eq. (6) is applicable to external or internal flows respectively and  $R$  is the local perpendicular distance from the axis of symmetry to the body surface. Utilizing this differential area in Eqs. (1) and (2) results in the following expressions for the displacement and momentum thickness

$$r\delta^* + \delta^* - \int_0^1 (1 - \beta u) (1 + 2r\eta) d\eta = 0 \quad (8)$$

and:

$$r\theta + \theta - \int_0^1 \beta u (1 - u) (1 + 2r\eta) d\eta = 0 \quad (9)$$

Two-dimensional flows are embedded in this general formulation as the limiting case of  $r=0$ , where

$$r = \pm \delta \cos \alpha / D \quad (10)$$

and the  $\pm$  sign carries the same significance as previously noted. Since  $r$ ,  $\delta^*$  and  $\theta$  are significantly less than unity for the majority of cases of interest, Eqs. (8) and (9) can generally be approximated by

$$\delta_o^* = \int_0^1 (1 - \beta u) d\eta \quad (11)$$

and

$$\theta_o = \int_0^1 \beta u (1 - u) d\eta \quad (12)$$

Upon integrating the axisymmetric equations of motion across the boundary layer (Ref. 1), the resulting momentum integral equation explicitly involves the terms  $H_o$  and  $\theta_o$  in the form

$$\frac{d\theta_o}{dx} + \theta_o \left\{ \frac{dH_o}{dx} (H_o + 2 - M_o^2) + \frac{d \ln D}{dx} \right\} = \frac{C_f}{2} \quad (13)$$

where

$$H = \delta^* / \theta_o \quad (14)$$

and  $\delta_o^*$  and  $\theta_o$  (i.e.  $\delta_{2D}^*$  and  $\theta_{2D}$ ) are calculated from the dimensional counterparts of Eqs. (11) and (12).

It is now apparent that the uniformly valid physical descriptions of the displacement and momentum thickness, as expressed mathematically by Eqs. (1) and (2), supply relationships which are identical to those appearing in the governing momentum integral equations for values of  $r$  generally encountered. However, for cases of large  $r$  with flowfield conditions which generate large values of  $\delta^*$  and  $\theta$ , Eqs. (8) and (9) should be applied when calculating the integral thickness parameters which have been described physically ( $\delta^*$ ,  $\theta$ ), while the appropriate forms of  $\delta_o^*$  and  $\theta_o$  are utilized in the solution of the equations of motion.

The principal point of this Note is to emphasize those situations in which the terms  $\delta^*$  and  $\theta$  are being considered.

apart from their relationship to terms appearing in the governing conservation equations, and in which the expressions generally employed for their evaluation are those appropriate to  $\delta^*$  and  $\theta$ . For example, consistent empirical correlation of the skin friction coefficient with momentum thickness and the shape factor with the various independent flowfield parameters should extend more universally into the large  $\tau$  domain utilizing the general expressions contained in Eqs. (8) and (9). In addition, the use of displacement thickness distributions to generate "effective bodies" in hypersonic flow utilizing the tangent cone approximation or in the study of the entry region of an axisymmetric pipe flow would benefit from the use of Eqs. (8) and (9) which result directly from the simple physical descriptions of displacement and momentum thicknesses.

The results of the investigation reported here provide general indications of the limits on  $\tau$  for which the terms  $\theta$ ,  $\delta^*$ , and  $H$ , that arise from the integral conservation equations are valid measures of  $\bar{\theta}$ ,  $\bar{\delta}^*$  and  $\bar{H}$  which have their basis in the development leading to Eqs. (1) and (2). Given the dependence of  $\bar{\theta}$ ,  $\bar{\delta}^*$  and  $\bar{H}$  on  $\tau$  and the parameters which characterize the flowfield, the values of  $\theta$ ,  $\delta^*$  and  $H$  can be obtained from the following relations, derivable from Eqs. (8), (9), (11), and (12):

$$\frac{\theta_w - \bar{\theta}}{\bar{\theta}} = \tau \bar{\theta} \quad (15a)$$

$$\frac{\delta_w^* - \bar{\delta}^*}{\bar{\delta}^*} = \tau \bar{\theta} H \quad (15b)$$

$$\frac{H_w - H}{H} = \frac{\tau \bar{\theta}}{1 + \tau \bar{\theta}} (H - 1) \quad (15c)$$

These equations also provide the percentage difference between the two sets of integral thickness variables of interest.

In order to determine the quantitative effect of  $\tau$  on the displacement and momentum thicknesses for a representative case of interest, the following formulas for the distributions of velocity and temperature through a constant pressure turbulent boundary layer have been utilized:

$$u = u^* \quad (16a)$$

$$T = a + b q^{1-\alpha} + c q^{1-\beta} \quad (16b)$$

For these computations, the term  $\epsilon$  in the coefficient  $b$  of Eq. (16b), which characterizes the lack of similarity between the velocity and temperature fields for Prandtl numbers different from one, has been set equal to unity.

If it is assumed that the pressure is constant across the boundary layer (another aspect of large  $\tau$  layers to be quantitatively evaluated), Eq. (16) can be applied to Eqs. (8) and (9) and the resultant integral parameters computed as a function of the principal independent flowfield variables

$$\bar{\theta}, \bar{\delta}^*, H = \bar{\theta}, \bar{\delta}^*, H(\gamma, Pr, T_w, M_\infty, N; \tau) \quad (17)$$

The effects of  $\gamma, Pr, M_\infty$  and  $N$  did not significantly affect the specification of a characteristic  $\tau$  for which the integral boundary-layer characteristics, as evaluated by Eqs. (8) and (9), depart from the values calculated from Eqs. (11) and (12). Therefore, at  $M_\infty = 2$  and  $N = 7$ , the influence of  $T_w$  and  $\tau$  on the integral parameters  $\bar{\theta}$  and  $\bar{H}$  has been computed for air with  $\gamma = 1.4$  and  $Pr = .72$  as shown in Fig. 1. The data encompass a wide range of values for  $\tau$  and  $T_w$ , not because they are physically likely to occur but solely to expose the variable dependences of interest.

Mach numbers from 0-4 and power-law exponents from 5-10 all exhibited curves of similar shape. At higher Mach numbers the sensitivity of  $H$  to  $\tau$  for cold wall conditions

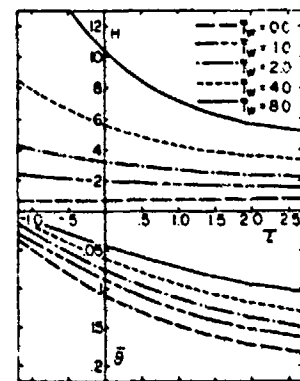


Fig. 1 Dependence of  $\bar{\theta}$  and  $\bar{H}$  on  $\tau$  and  $T_w$  for a constant pressure turbulent boundary layer.  $M_\infty = 2$ ,  $N = 7$ ,  $\gamma = 1.4$  and  $Pr = 0.72$ .

becomes increasingly positive while the shift in position of the curves for a varying  $N$  amounted to a few percent for each integer change in the exponent.

Utilizing the results presented in Fig. 1 and Eqs. (15), the percentage difference between the two displacement thicknesses at  $\tau = 1.0$  and  $T_w = 4.0$  has been calculated to be 40% while the shape factors differ by 28%. It is thus clear that, for high  $\tau$  boundary layers, utilization of the physically describable entities  $\bar{\delta}^*$  and  $\bar{\theta}$  must be carefully distinguished from the terms  $\delta_w^*$  and  $\theta_w$  which arise in the governing integral conservation equations.

To this point, other commonly used integral boundary-layer thicknesses (Ref. 3) have been neglected, inasmuch as their usefulness lies primarily in the fact that they allow the governing equations to be presented in a compact formulation. Their application to procedures outside the scope of solving the equations is relatively limited. One infrequent exception is the use of the enthalpy thickness ( $\delta_h$ ) to correlate the dependence of the Stanton number on the Reynolds number,  $Re_{\delta_h}$ , as shown in Ref. 2.

The enthalpy thickness can be introduced on a purely physical basis in a manner identical to that used for the momentum thickness. The resulting mathematical expression for this physical entity is

$$\tau \bar{\theta}_h^2 + \delta_h - \int_0^{\tau} \Delta u (N-1) (1+2\tau q) dq = 0 \quad (18)$$

By integrating the axisymmetric energy equation through the boundary layer, the term  $\delta_h$  arises naturally from the integration procedure, where

$$\delta_h = \int_0^{\tau} \Delta u (N-1) (1+2\tau q) dq \quad (19)$$

Eq. (18) can therefore be written:

$$\tau \bar{\theta}_h^2 + \delta_h - \delta_h = 0 \quad (20)$$

However, for a perfect gas boundary-layer flow with constant pressure across the viscous region, it is possible to show that

$$\delta_h = \bar{\delta}^* - \int_0^{\tau} (1-u) (1+2\tau q) dq \quad (21)$$

If a velocity profile of the form presented in Eq. (16) is utilized, Eq. (21) results in

$$\delta_h = \bar{\delta}^* - \left[ \frac{N + (1+\tau)(N+1)}{(N+1)(2N+1)} \right] \quad (22)$$

Therefore, the generalized enthalpy thickness, with which the convective heat transfer is to be correlated, may be computed from Eq. (20), written in the form

$$\delta_h = (-1 + \sqrt{1 + 4\tau \bar{\theta}_h}) / 2\tau \quad (23)$$

with  $\bar{\delta}_{\tau,0}$  being evaluated utilizing Eq. (22) and the results of computations similar to those presented in Fig. 1.

Finally, the generalized definitions for each of the integral thicknesses employed here are compatible with the limiting case of axial boundary-layer flow over a needle. In this situation  $\tau$  approaches infinity and each of the integrals reduces to the form of the following equation for displacement thickness

$$\bar{\delta}^*_{\tau,1} = \left( \int_0^1 (1 - \bar{u}) d\eta^2 \right)^{1/2} \quad (24)$$

#### Acknowledgment

The author would like to acknowledge the very helpful critique provided by F.E.C. Culick.

#### References

- <sup>1</sup>Scholkemeier, F.W., Die laminare Reibungsschicht an rotationssymmetrischen Körpern, *Archiv der Mathematik*, Vol. 1, 1949, pp. 270-277.
- <sup>2</sup>Kutateladze, S.S., Leont'ev, A.I., "Boundary Layers in Compressible Gases," translated by Spalding, D.B., Academic Press, New York, 1964.
- <sup>3</sup>Schlichting, H., *Boundary Layer Theory*, 6th edition, McGraw-Hill, New York, 1968.

With this justification, the solid bodies which support the optimum viscous displacement bodies may be established by first computing the displacement thickness and then subtracting it from the optimum shape. This procedure is necessarily iterative inasmuch as, although the inviscid pressure field is known, the solid surface is not. Therefore, the location of the surface boundary conditions is also unknown. The iteration begins by assuming, initially, that the solid body shape is the computed optimum shape. The resultant boundary layer displacement is then subtracted from the optimum shape and the entire procedure is repeated. At high Reynolds number, convergence is obtained within a few cycles. At low Reynolds number, convergence may be ensured only by partially correcting the first guess solid body shape so as to ensure that a large overshoot does not occur.

Computation of the viscous flow displacement and skin friction at each iteration is carried out within the framework of the following equations, utilizing standard notation.

# THE HOKENSON COMPANY

## AXISYMMETRIC GOVERNING EQUATIONS OF MOTION

$$\frac{\partial U}{\partial t} + \frac{\partial F}{\partial x} + \frac{1}{r} \frac{\partial}{\partial r} (r G) = j \frac{H}{r}$$

$$U = \begin{bmatrix} \rho \\ \rho u \\ \rho v \\ \rho e \end{bmatrix} \quad F = \begin{bmatrix} \rho u \\ \rho u^2 - \sigma_{xx} \\ \rho uv - \tau_{xy} \\ \rho ue + \dot{q}_x - u\sigma_{xx} - v\tau_{xy} \end{bmatrix} \quad G = \begin{bmatrix} \rho v \\ \rho uv - \tau_{xy} \\ \rho v^2 - \sigma_{rr} \\ \rho ve + \dot{q}_r - u\tau_{xy} - v\sigma_{rr} \end{bmatrix} \quad H = \begin{bmatrix} 0 \\ 0 \\ -\sigma_H \\ 0 \end{bmatrix}$$

$$\sigma_{xx} = -P + (\lambda + \lambda_r) \nabla \cdot V + 2(\mu + \epsilon) \frac{\partial u}{\partial x}$$

$$\sigma_{rr} = -P + (\lambda + \lambda_r) \nabla \cdot V + 2(\mu + \epsilon) \frac{\partial v}{\partial r}$$

$$\sigma_H = -P + (\lambda + \lambda_r) \nabla \cdot V + 2(\mu + \epsilon) \frac{v}{r}$$

$$\tau_{xy} = (\mu + \epsilon) \left( \frac{\partial u}{\partial r} + \frac{\partial v}{\partial x} \right)$$

$$\dot{q}_x = -C_p \left( \frac{\mu}{Pr} + \frac{\epsilon}{Pr_r} \right) \frac{\partial T}{\partial x}$$

$$\dot{q}_r = -C_p \left( \frac{\mu}{Pr} + \frac{\epsilon}{Pr_r} \right) \frac{\partial T}{\partial r}$$

$$(\lambda + \lambda_r) = -\frac{1}{2}(\mu + \epsilon)$$

Once the solid body shapes have been computed, the internal volume distribution may be calculated. During Phase I, a simple right circular cylindrical penetrator shape was assumed. The maximum volume of such a cylinder which can fit within the solid body shape divided by the total body volume is defined as the prismatic coefficient, P. During subsequent work other reference penetrator shapes, including dual in-line cylinders of different diameter, may be considered.

The loss in kinetic energy along the trajectory may then be computed from simple rigid body dynamics:

$$V/V_0 = \exp(-\tilde{\rho} \tilde{X} C_D/2)$$

where:

$V_0$  = launch velocity

$C_D$  = average  $C_D$  along  $\tilde{X}$

$\tilde{X} = X/L_{ref}$

$X$  = length of flight

$L_{ref}$  = total volume/base area

$\tilde{\rho}$  = ambient density/average projectile density

For preliminary computations, the average projectile density may be approximated as the prismatic coefficient, P, times the density of the penetrator. Therefore, for a given length of flight, ambient density and penetrator material density, the minimum velocity degradation is associated with minimizing:

$$C_D/P$$

It is clear that  $L_{ref}$  varies from shape to shape so that the actual degradation in velocity, even for a given range and equal  $C_D/P$ , changes also.

Unfortunately, the competition between candidate shapes is not quite so straightforward when real-life operational considerations are introduced. For example, the launch device 'barrel' may constrain the base diameters to be equal. In addition, we may insist on comparing projectiles with the same total launch mass. Again neglecting the residual projectile structure, the total mass may be written:

$$m = \rho_{pen.} A L_{ref} P$$

If only the base areas of candidate projectiles must be equal, their masses will vary as the product of

$$P \times L_{ref}$$

for the same penetrator density. If, however, the masses must also be equal, then the product:

$$P \times L_{ref}$$

must be constant. This may be effected by varying the aspect ratio of the computed optimal configurations from shape to shape\*. Clearly, aspect ratio, mass and base area

\*In so doing, however, projectile stability considerations for a given spin or fin geometry also restrict the acceptable range of aspect ratio.

may not all be constrained. (A somewhat artificial way out of this problem is to assume that any ullage will be filled with exactly that amount of (non-penetrator) mass required to make the payload masses equal.) For purposes of the Phase I work, it is sufficient to require the masses and aspect ratios to be equal for all candidate shapes. The base areas shall then vary inversely as the product:

$$P \times L_{\text{ref}}$$

As a result, any launch device 'barrel' diameter constraint is ignored.

The final 'real-life' problem is the requirement to compute  $C_D$  at off-design Mach and Reynolds numbers in order to determine its average value along the trajectory.

Given the ability to predict the momentum and kinetic energy of the projectile at the target location, the details of the initial stages of impact are computed from the Navier-Stokes equations utilizing physical properties appropriate to the materials involved<sup>2,3</sup>:

# THE HOKENSON COMPANY

## TRANSIENT MULTI-DIMENSIONAL EQUATIONS OF MOTION

$$\frac{\partial U}{\partial t} + \frac{\partial F}{\partial x} + \frac{\partial G}{\partial y} + \frac{\partial H}{\partial z} = 0$$

$$U = \begin{bmatrix} \rho \\ \rho u \\ \rho v \\ \rho w \\ \rho E \end{bmatrix}$$

$$F = \begin{bmatrix} \rho u \\ \rho u u - \tau_{11} \\ \rho u v - \tau_{12} \\ \rho u w - \tau_{13} \\ \rho E u - K \frac{\partial T}{\partial x} - (u \tau_{11} + v \tau_{12} + w \tau_{13}) \end{bmatrix}$$

$$G = \begin{bmatrix} \rho v \\ \rho u v - \tau_{12} \\ \rho v v - \tau_{22} \\ \rho v w - \tau_{23} \\ \rho E v - K \frac{\partial T}{\partial y} - (u \tau_{12} + v \tau_{22} + w \tau_{23}) \end{bmatrix}$$

$$H = \begin{bmatrix} \rho w \\ \rho u w - \tau_{13} \\ \rho v w - \tau_{23} \\ \rho w w - \tau_{33} \\ \rho E w - K \frac{\partial T}{\partial z} - (u \tau_{13} + v \tau_{23} + w \tau_{33}) \end{bmatrix}$$

$$\tau_{ij} = \delta_{ij} P - \mu \left( \frac{\partial W_i}{\partial X_j} + \frac{\partial W_j}{\partial X_i} - \frac{2}{3} \delta_{ij} \frac{\partial W_k}{\partial X_k} \right)$$

Following the work of MacCormack<sup>4</sup>, the momentum transfer to the target may be computed in order to quantify the target damage. Typical results for a cylindrical penetrator are discussed in the next section.

## Results and Conclusions

On the basis of the Newton-Busemann pressure equation, the optimal viscous displacement body configurations for five different cases were obtained. The results are presented in the following figures for an overall aspect ratio of five. Since the projectile mass is constant from case to case, the base area is assumed to vary inversely as  $P \times L_{ref}$  for a given penetrator shape and density.

Once the displacement body shape was obtained, state-of-the-art turbulent boundary layer computations were carried out in an iterative mode for the following conditions:

$$M = 5.0 \quad ,$$
$$Re_{\infty} = 10^6 \quad , \text{ and}$$

Smooth adiabatic wall.

As a result of the iteration, a consistent combination of  $\delta^*$  and body radius whose sum equalled the computed optimum shape, was converged upon. Due to time and cost constraints, lower Reynolds numbers and thicker boundary layers were not considered due to their slow rate of convergence.

The resultant  $C_D$  (inviscid plus viscous on the forebody) and  $P$  are shown on each figure with which the velocity degradation may be assessed. In order to account for fin stabilization, an additional  $C_D$  increment is required. For spin stabilization, the aforementioned boundary layer computation has been modified to allow the displacement thickness subtraction process and skin friction computation to be carried out. Typical results for the conical body at two spin rates are presented in Figures 7a - 7d.

For an aluminum penetrator, with a length to diameter ratio of one, impacting a semi-infinite aluminum target, typical results of a Navier-Stokes simulation of the initial stages of impact are depicted in Figure 8. On the basis of the various fluxes of momenta, target damage effectiveness may be quantified.

As a result of the Phase I work, it is clear that a systematic consideration of (inviscid and viscous) drag, internal volume distribution and impact effectiveness is feasible in order to establish optimal hypervelocity projectile shapes. Subsequent wind tunnel validation of the results from an extended application of this analysis is required prior to the execution of ballistic range and impact experiments.

## References

1. Eggers, A.J., Resnikoff, M.M. and Dennis, D.H., "Bodies of Revolution Having Minimum Drag at High Supersonic Airspeeds," NACA Rep. 1306, 1957.
2. Tillotson, J.H., "Metallic Equations of State for Hypervelocity Impact," General Atomic Report GS-3216, 1962.
3. Sakharov, A.D., Zaidel, R.M., Miniev, V.N. and Oleinik, A.G., "Experimental Investigations of the Stability of Shock Waves and the Mechanical Properties of Substances at High Pressures and Temperatures," Soviet Physics, Doklady, Vol. 9, No. 12, June 1965.
4. Mac Cormack, R.W., "The Effect of Viscosity in Hypervelocity Impact Cratering," AIAA Paper No. 69-354.

Table 1.

Minimum Drag Projectile Design Cases Studied

Case 1.: Figures 2a & 2b: Given length and base diameter.

Case 2.: Figures 3a & 3b: Given length and volume.

Case 3.: Figures 4a & 4b: Given length and surface area.

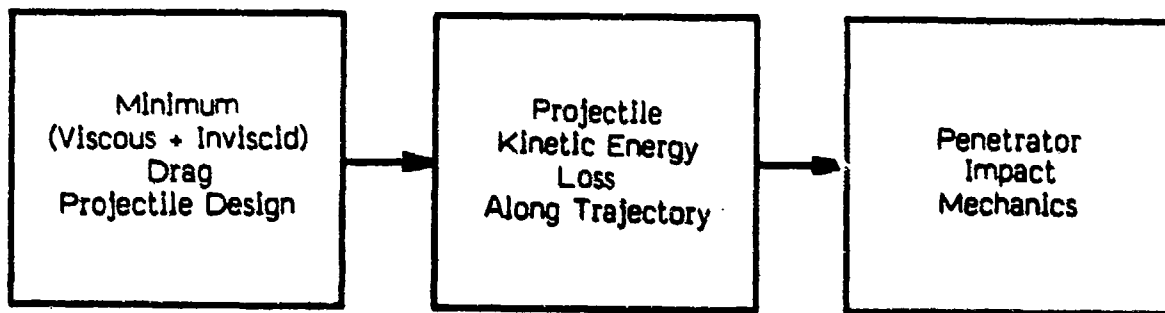
Case 4.: Figures 5a & 5b: Given base diameter and volume.

Case 5.: Figures 6a & 6b: Given base diameter and surface area.

Case 6.: Figures 7a - 7b: Case 6 with two spin rates

Figure 1.

Schematic of Optimization Considerations



Case 1.

Minimum Drag Shape for a Given Length and Base Diameter

Figure 2a.: Original and corrected shapes.

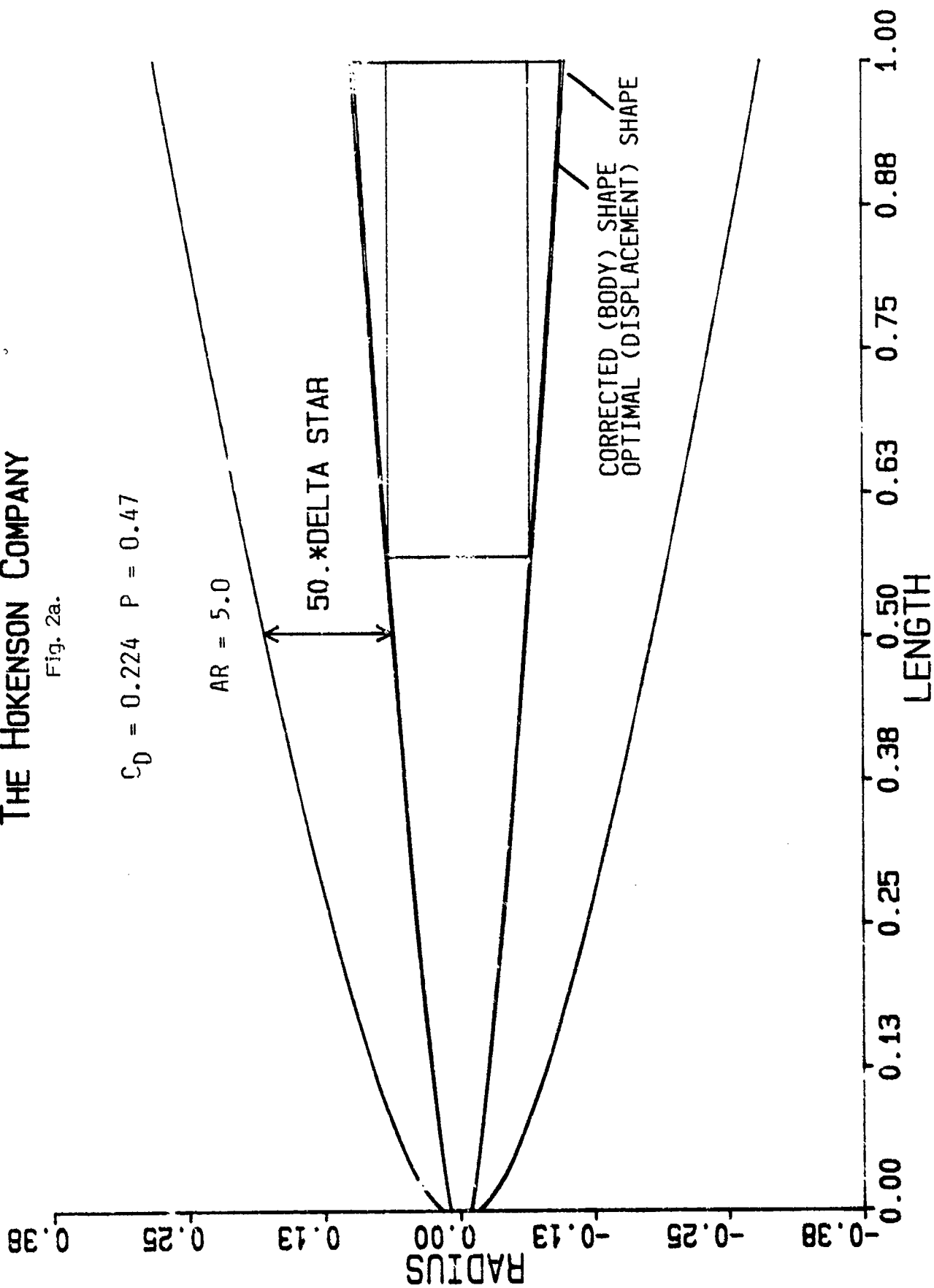
Figure 2b.: Skin friction and pressure distributions.

THE HOKENSON COMPANY

Fig. 2a.

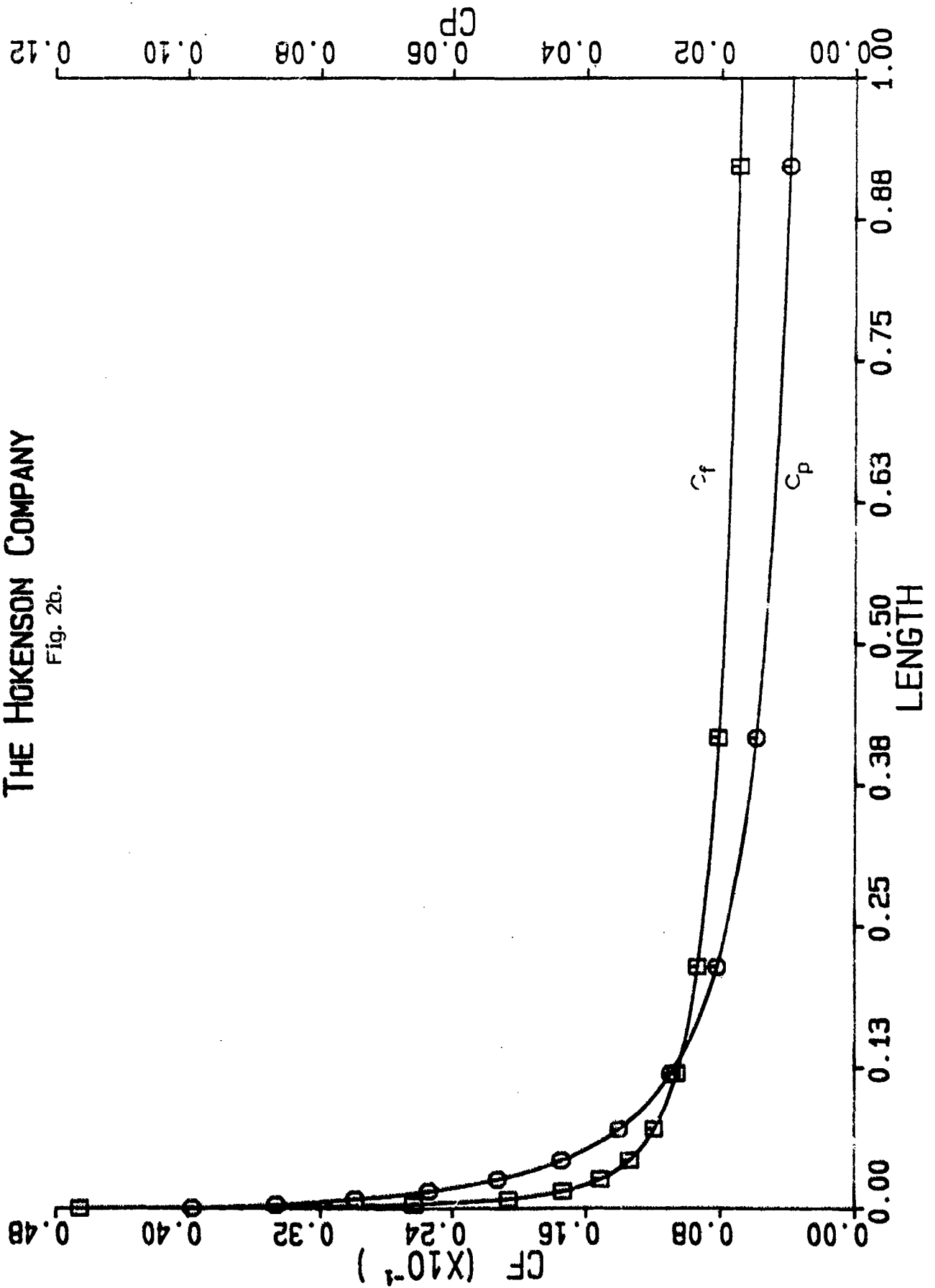
$$C_D = 0.224 \quad P = 0.47$$

$$AR = 5.0$$



THE HOKENSON COMPANY

Fig. 2b.



Case 2.

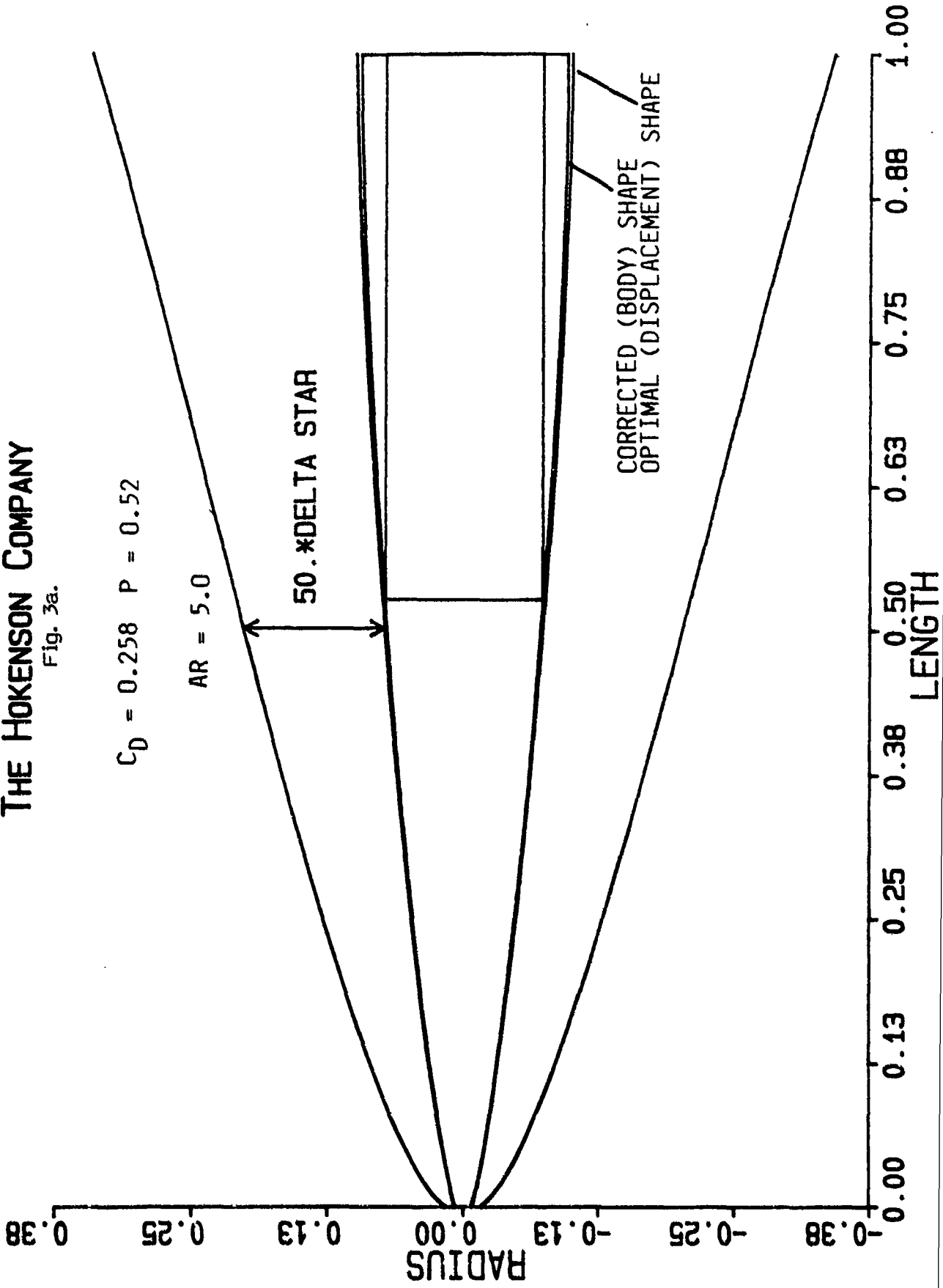
Minimum Drag Shape for a Given Length and Volume

Figure 3a.: Original and corrected shapes.

Figure 3b.: Skin friction and pressure distributions.

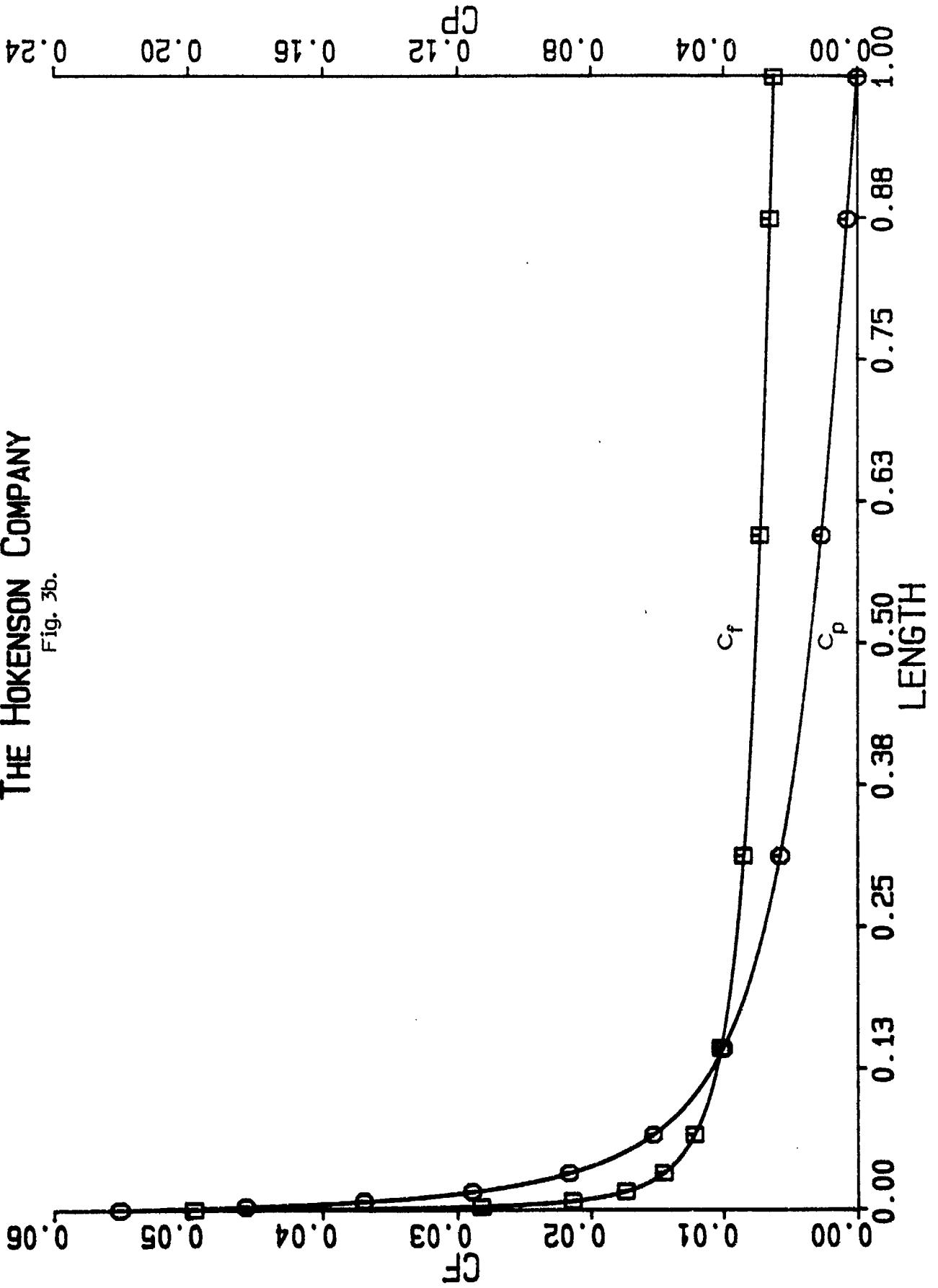
THE HOKENSON COMPANY

Fig. 3a.



THE HOKENSON COMPANY

Fig. 3b.



Case 3.

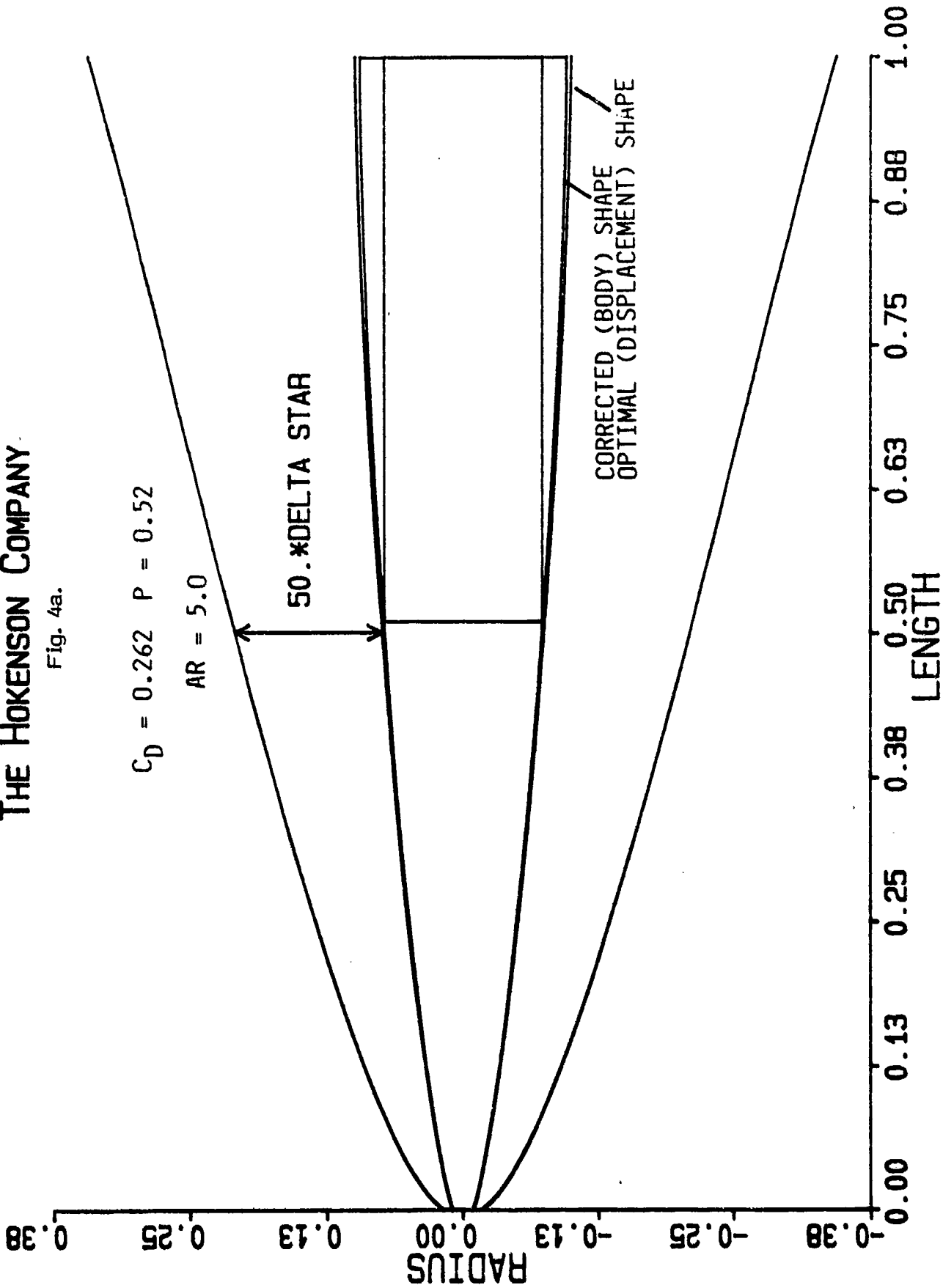
Minimum Drag Shape for a Given Length and Surface Area

Figure 4a.: Original and corrected shapes.

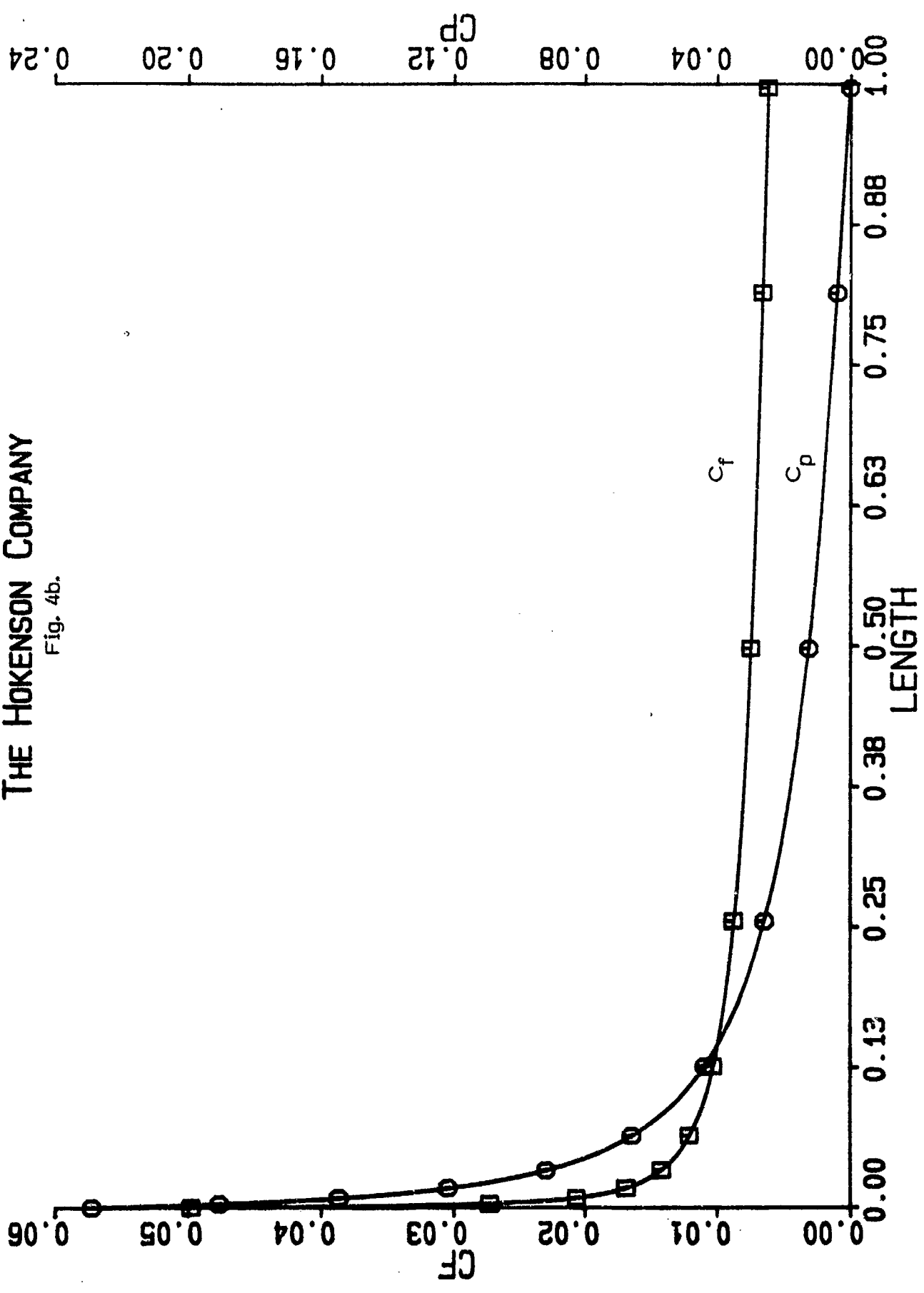
Figure 4b.: Skin friction and pressure distributions.

THE HOKENSON COMPANY

Fig. 4a.



THE HOKENSON COMPANY  
Fig. 4b.



Case 4.

Minimum Drag Shape for a Given Base Diameter and Volume

Figure 5a.: Original and corrected shapes.

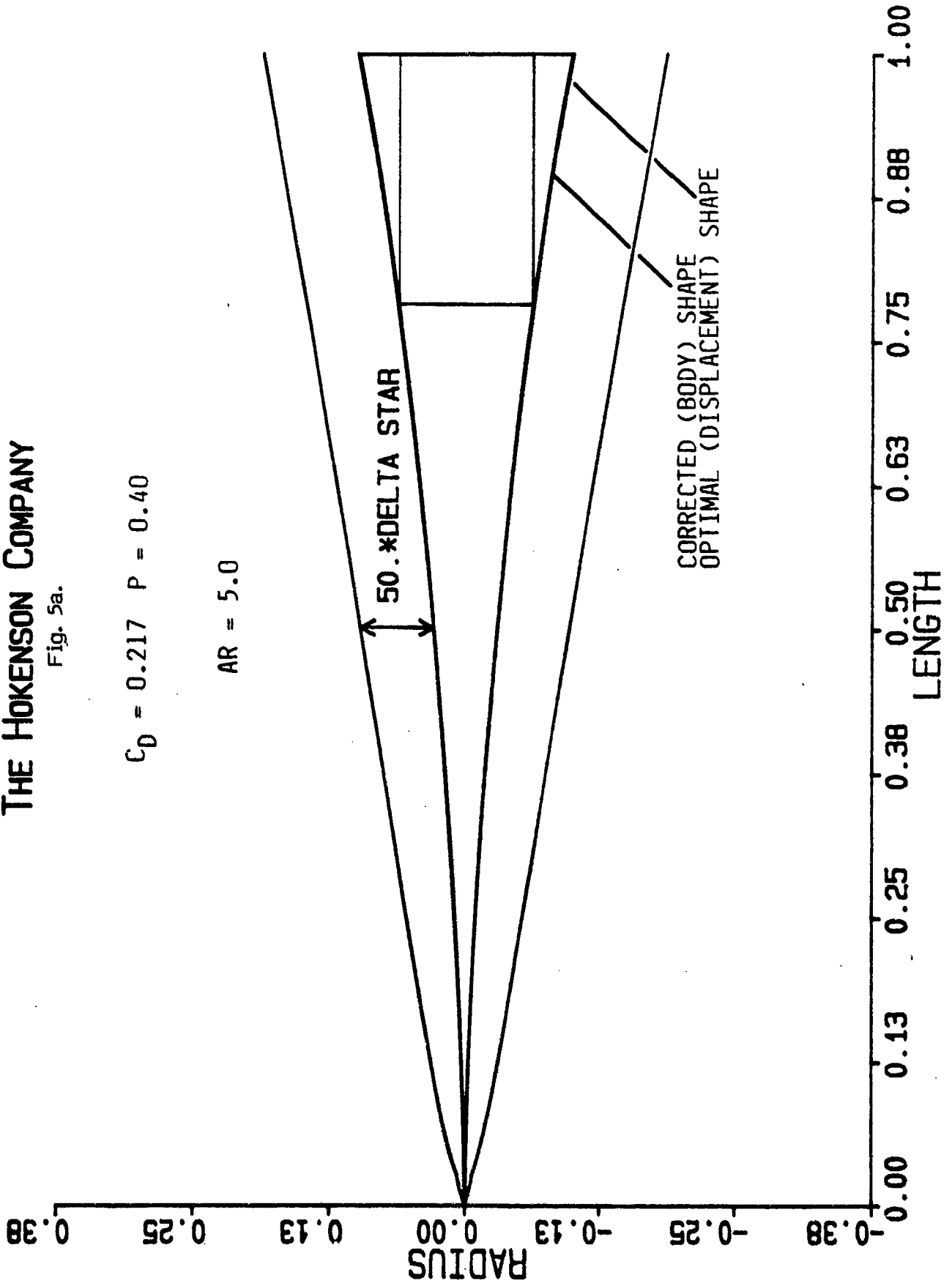
Figure 5b.: Skin friction and pressure distributions.

THE HOKENSON COMPANY

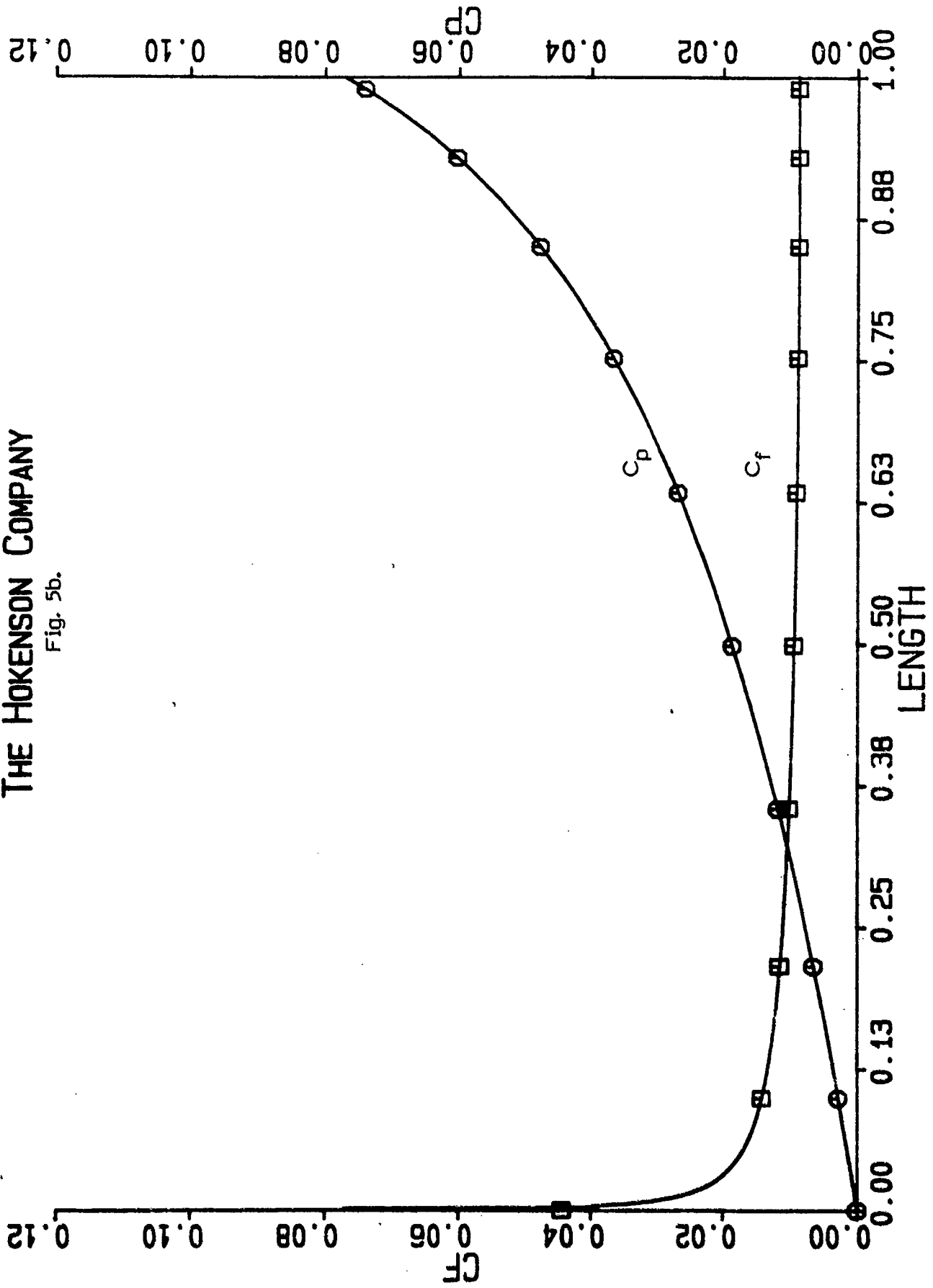
Fig. 5a.

$$C_D = 0.217 \quad P = 0.40$$

$$AR = 5.0$$



THE HOKENSON COMPANY  
Fig. 5b.



Case 5.

Minimum Drag Shape for a Given Base Diameter and Surface Area

Figure 6a.: Original and corrected Shapes.

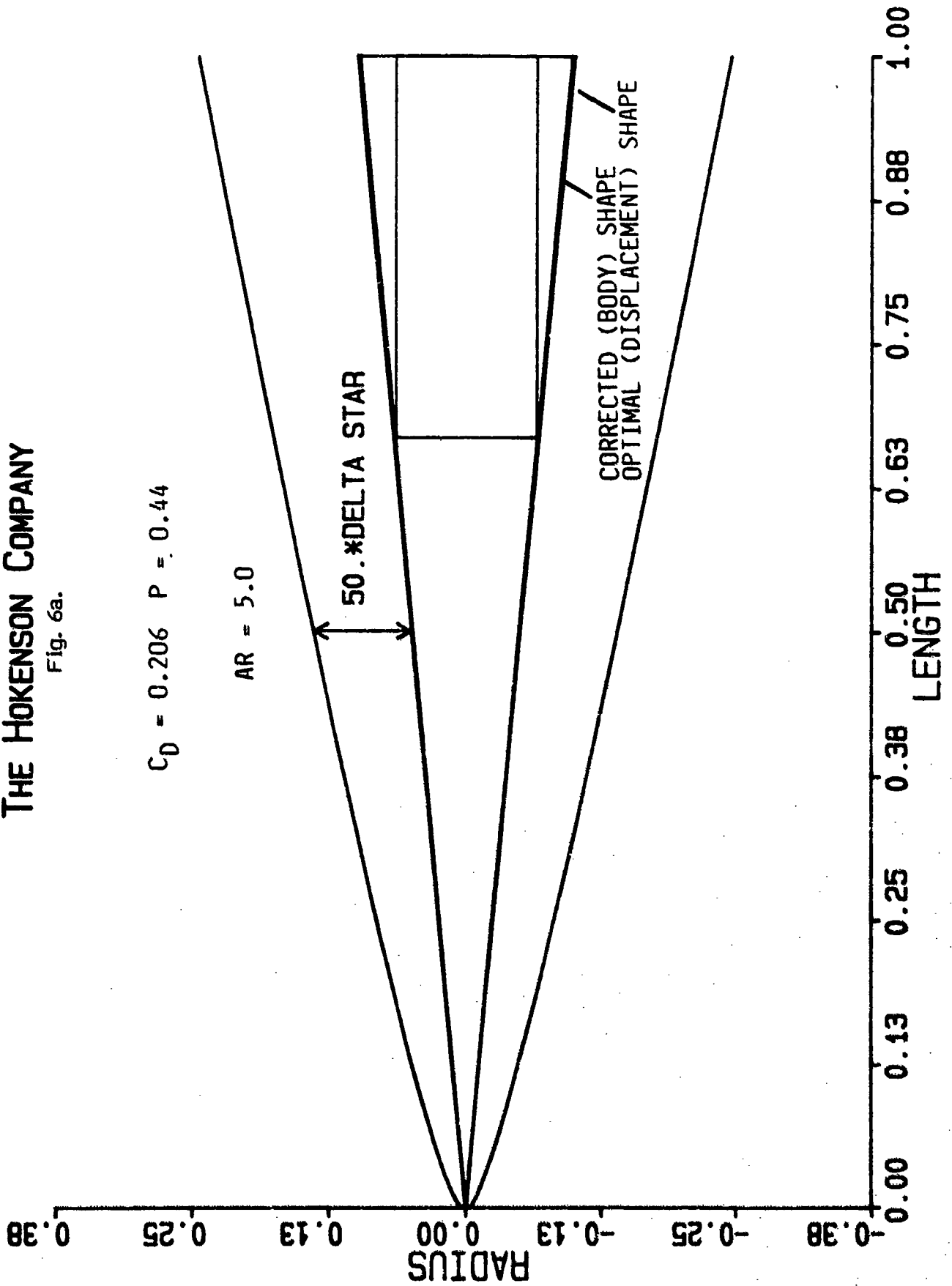
Figure 6b.: Skin friction and pressure distributions.

THE HOKENSON COMPANY

Fig. 6a.

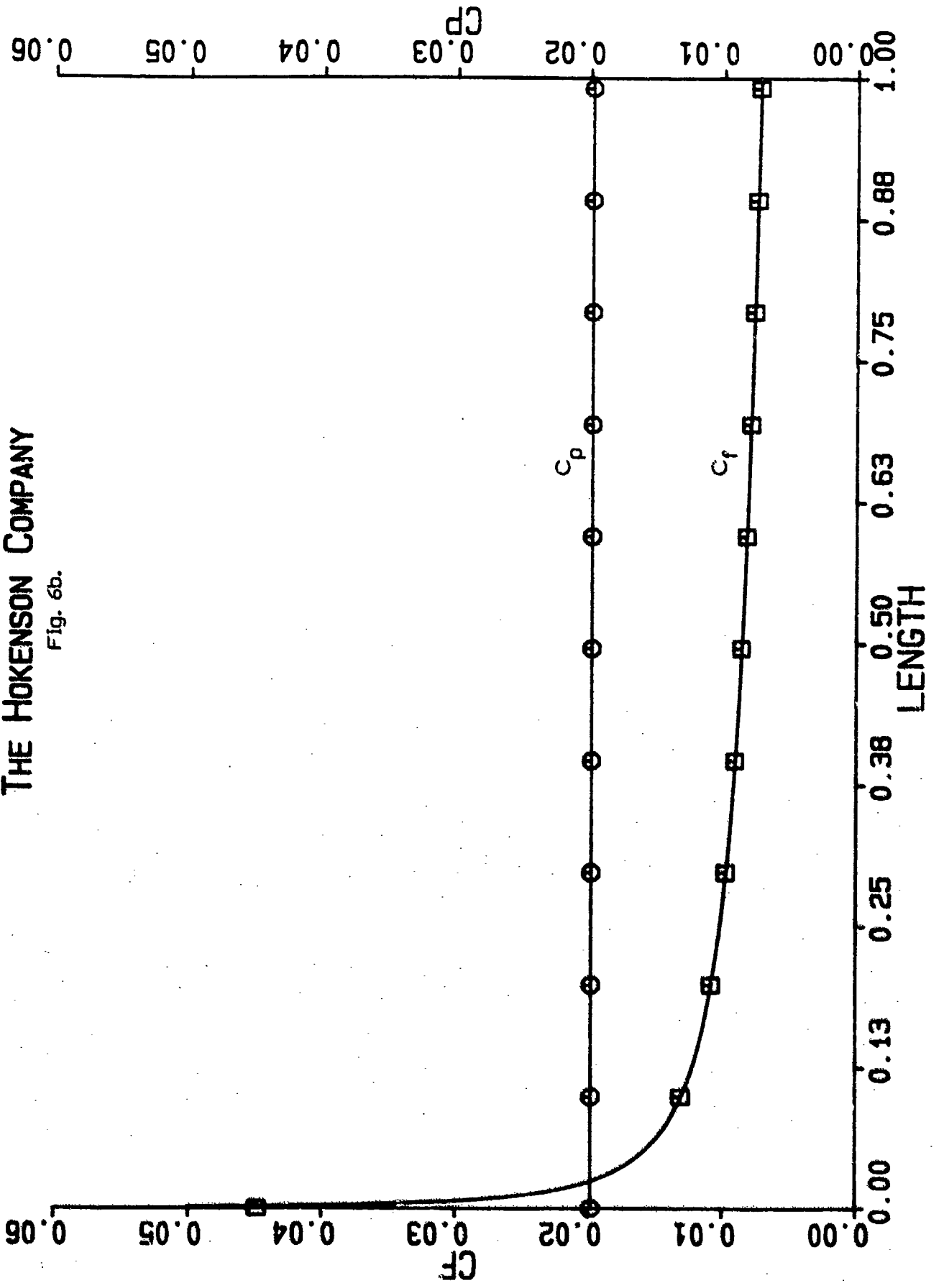
$$C_D = 0.206 \quad P = 0.44$$

$$AR = 5.0$$



THE HOKENSON COMPANY

Fig. 6b.



Case 6.

Case 5. Repeated with Body Rotation

Figure 7a.: Original and corrected shapes at a spin rate of  $2 \times 10^5$  rpm.

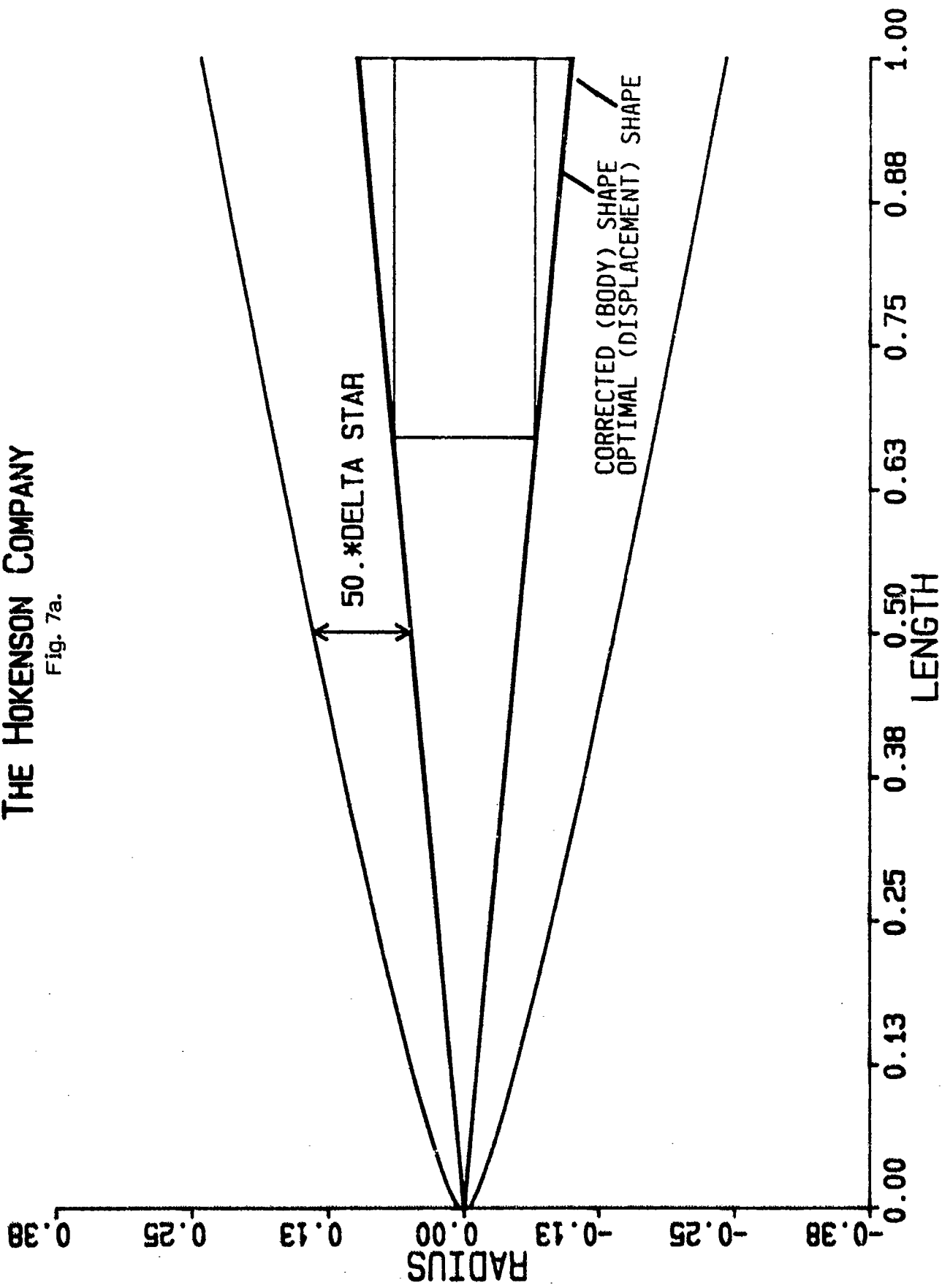
Figure 7b.: Skin friction and pressure distributions at a spin rate of  $2 \times 10^5$  rpm.

Figure 7c.: Original and corrected shapes at a spin rate of  $1 \times 10^5$  rpm.

Figure 7d.: Skin friction and pressure distributions at a spin rate of  $1 \times 10^5$  rpm.

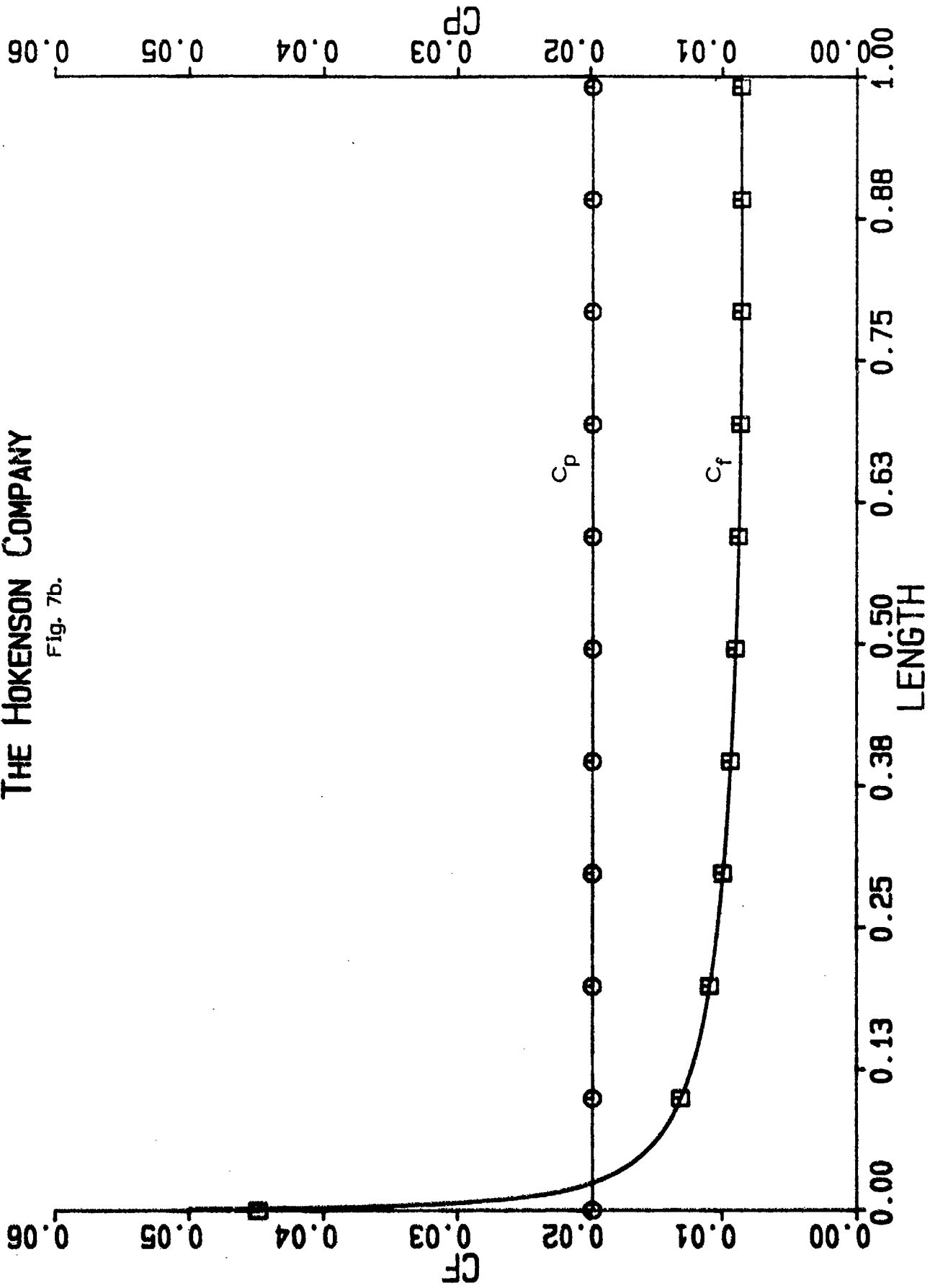
THE HOKENSON COMPANY

Fig. 7a.



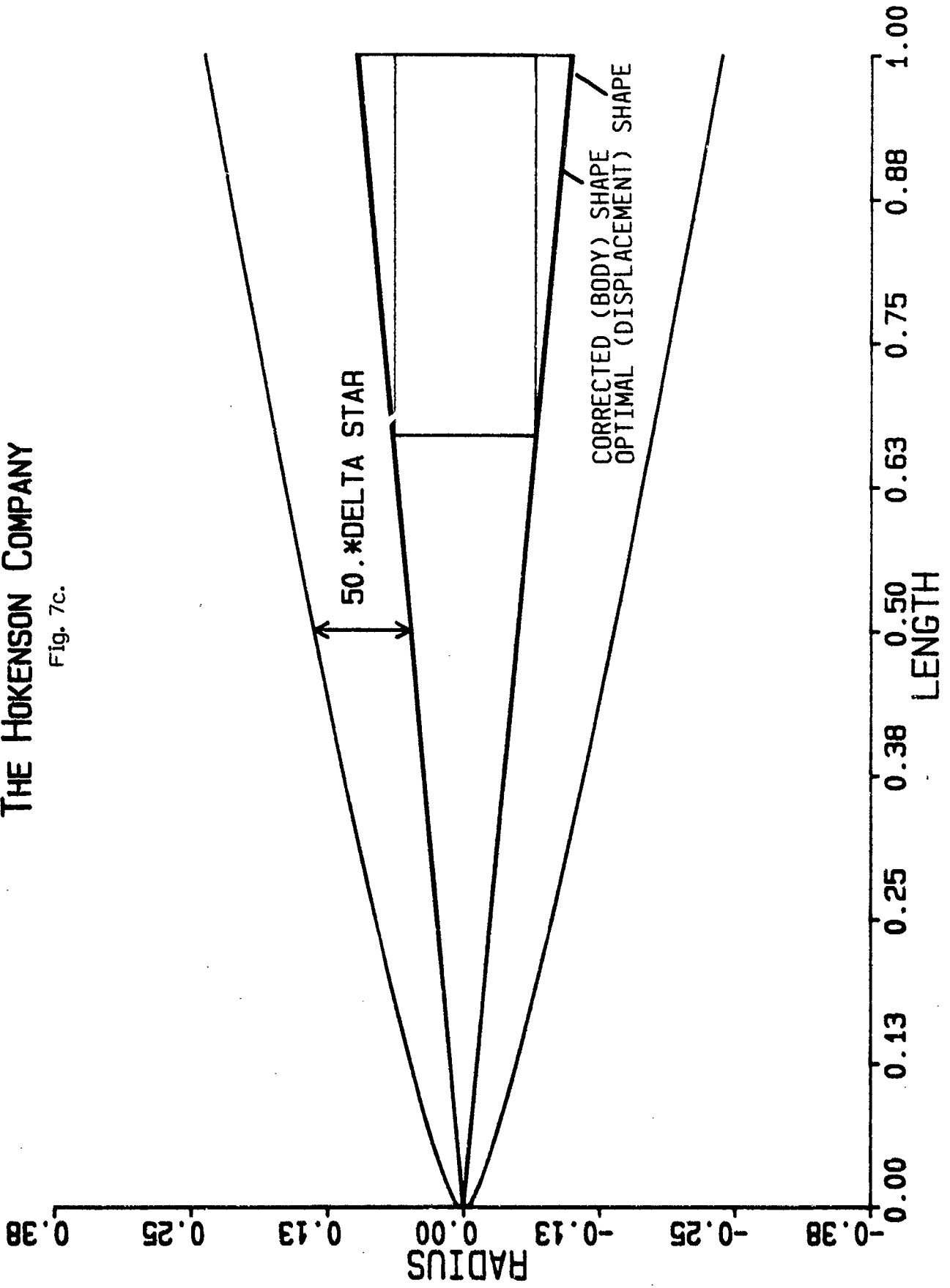
THE HOKENSON COMPANY

Fig. 7b.



THE HOKENSON COMPANY

Fig. 7c.



THE HOKENSON COMPANY  
Fig. 7d.

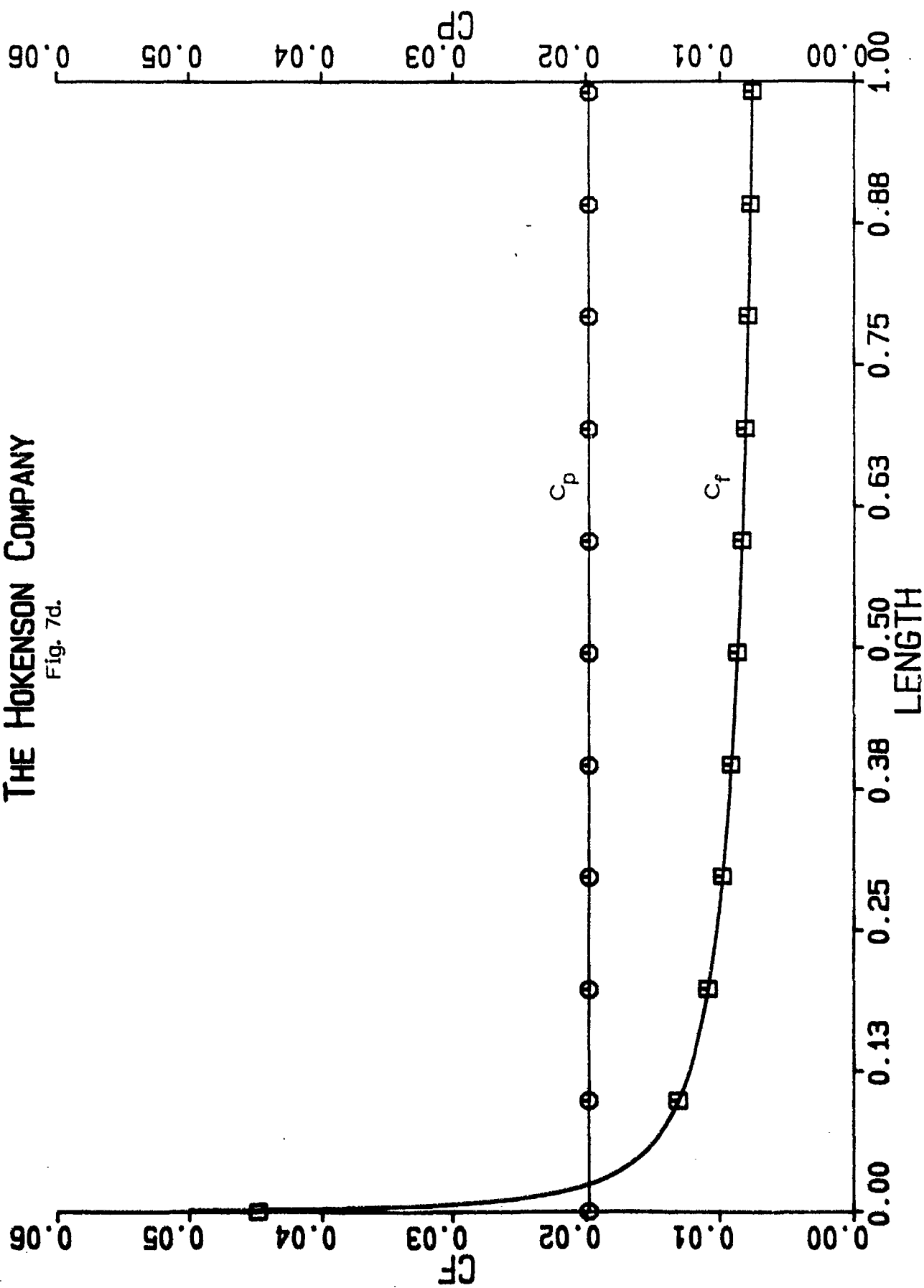
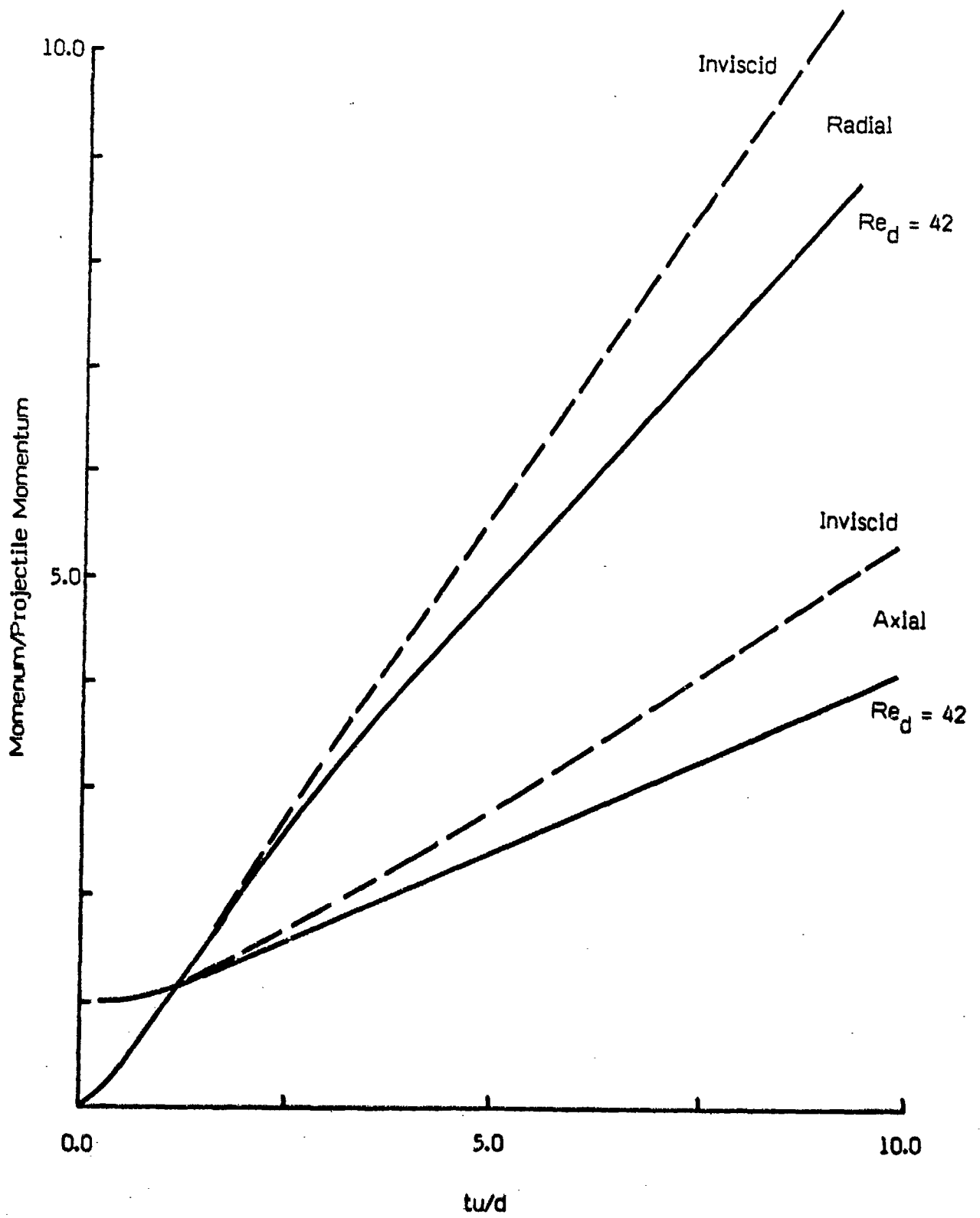


Figure 8. Navier-Stokes Impact Solution For Cylindrical Penetrator



Appendix

Optimal Design Publications of the Principal Investigator

# Unified Inlet/Diffuser Design by an Inverse Method

G. J. Hokenson\*

STD Research Corporation, Arcadia, Calif.

and

F. Y. Su†

Science Applications Inc., La Jolla, Calif.

The equations governing the two-dimensional, steady, inviscid flow of an incompressible fluid have been formulated in an inverse manner to obtain the resultant shape of semi-flush inlet/curved diffusers when the surface velocity distribution is specified. The results of calculations illustrating the effect of each of seven principal design variables on a nominal inlet configuration are presented. One of the configurations obtained was chosen for experimental testing to compare the on- and off-design performance of inlets generated by this procedure with that of inlets obtained by more conventional methods. General results and applications of this method are discussed.

## Nomenclature

$AR$	= area ratio, $h_r/h_i$
$d$	= vertical distance from inlet lip to ramp surface at $-\infty$ , (Fig. 1)
$DF$	= drop fraction, $d/h_i$
$h_i$	= vertical height of ramp above inlet lip, (Fig. 1)
$h$	= inlet height (Fig. 1)
$IVR$	= inlet velocity ratio, $U_i/U_\infty$
$K$	= inlet loss coefficient, $(P_{T_i} - P_{T_\infty})/q$ where: $q = q_i$ for $IVR > 1$ , $q = q_\infty$ for $IVR < 1$ .
$L$	= ramp length (Fig. 1)
$L_D$	= diffuser length (Fig. 1)
$LVR$	= lip velocity ratio, $U_{o_i}/U_\infty$
$\ln$	= natural base logarithm
$P_T$	= stagnation pressure
$q$	= dynamic pressure
$S_R$	= streamwise position, measured in inlet heights upstream from the lip, at which the ingested streamtube departs from a line which parallels the ramp (Fig. 1)
$u$	= component of velocity in $x$ direction
$U$	= velocity vector magnitude, $(u^2 + v^2)^{1/2}$
$v$	= component of velocity in $y$ direction
$x$	= horizontal Cartesian coordinate normalized by $L$ with origin at end of upstream uniform flow region
$y$	= vertical Cartesian coordinate normalized by $L$ with arbitrary origin
$\alpha$	= velocity vector angle, $\tan^{-1}(v/u)$
$\nabla_{\phi, \psi}^2$	= Laplacian operator in $\phi - \psi$ coordinates
$\delta$	= $\phi' / \phi_r$
$\Delta\phi$	= finite difference grid spacing in $\phi$
$\Delta\psi$	= finite difference grid spacing in $\psi$
$\phi$	= velocity potential; Eq. (5) and (6)
$\phi'$	= $\phi - \phi_r$
$\psi$	= stream function; Eq. (5) and (6)
$r$	= ingested streamtube length to height ratio, $L/h_\infty$ , (Fig. 1)
$r_D$	= diffuser length to height ratio, $L_D/h_i$
$\theta$	= lip angle with respect to the vertical (Fig. 1)
$w$	= $\psi_{i,j} / \psi_0$

## Subscripts

$e$	= conditions at diffuser exit
$i$	= streamline index
$o$	= conditions at $o$ (Fig. 2)
$r$	= conditions at $r$ (Fig. 2)
$s$	= conditions at $s$ (Fig. 2)
$\infty$	= conditions along ramp surface infinitely far upstream
$?$	= conditions at inlet lip (Fig. 3)
$1$	= lowest bounding streamline in computation region (Fig. 2)
$2,3$	= dividing streamline which splits at the lip (Fig. 2)
$4$	= streamline which forms ramp and upper surface of diffuser (Fig. 2)

## Introduction

INTAKE ducting in which an opening along a solid bounding surface to the flowfield is used to draw off fluid has been put to so many applications as to prohibit their explicit enumeration. Of prime importance among these applications are engine air inlets, auxiliary equipment inlets and boundary-layer suction slots, whether used in wind and water tunnels to "cleanse" the flow or to retard separation in a variety of adverse pressure gradient situations. For the majority of these inlet applications, a coupled diffuser is in evidence which allows the system to operate efficiently within the power constraints of the device which sustains the flow. Possibly equally as common is to have the diffuser curve

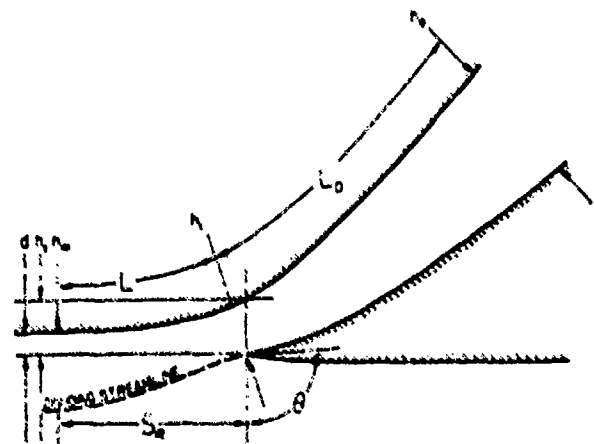


Fig. 1 Inlet configuration.

Received Jan. 5, 1976; revision received Aug. 12, 1976.

Index categories: Hydrodynamics; Subsonic and Transonic Flow

\*Group Manager and Senior Scientist, Physical Sciences Department, Formerly Supervisor and Senior Scientist, Waterjet Inlets, 2KSES Division, Rohr Industries, San Diego, Ca. Member AIAA

†Scientist, Formerly Senior Scientist, Waterjet Inlets, 2KSES Division, Rohr Industries, San Diego, Ca. Member AIAA

inboard from the flow surface along which the fluid is being drawn off. Initial experimental results obtained by the authors on inlets such as those shown in Fig. 1 indicate that the inlet geometry and flow conditions upstream of the lip, and to a finite but lesser extent on the downstream external lip, are strongly coupled to the pressure recovery and overall character of the flow inside the curved diffuser. This is not a particularly surprising fact, yet it is one which has received little intensive study. In general, the interaction effect of series/parallel hydrodynamically coupled components in a fluid system on the detailed flowfield is not yet understood. In engineering applications, established practice, guided by experience and some excellent classical experimental studies (e.g., Ref. 4-6), initiates the general design. Utilizing this procedure, many very efficient inlets have been developed after considerable empirical iteration on the design has been completed and which essentially compensates for these unknown interactions.

Dominant in the open literature with respect to their scope and intensity of experimental results are the publications of Mossman (e.g., Ref. 4) which, for inlet geometries of the general type investigated here, describe an optimum external pre-diffusion (indicated by an *IVR* less than one) for a given set of variations of a specific inlet configuration. These results have proved to be an invaluable guide in the development of inlets with relatively simple attached diffusers; however, the introduction of more complicated large-area-ratio, curved diffusers changes this picture significantly. The generation of curved diffuser shapes with relatively large expansions has been well documented in Ref. 3, supported by the analytical background developed in Ref. 1. The excellent experimental data obtained at Stanford<sup>2,3</sup> has served as a guide to the extent to which the boundary layers on each wall of a curved diffuser can support adverse pressure gradients, and indirectly the range of geometrical parameters which will result in an efficient pressure recovery device. There is little information available, however, which can serve as a guide to the unified design of an inlet/diffuser combination when large amounts of pre-diffusion, varying angle of incidence of the dividing streamline onto the inlet lip, and external lip geometry all interact with the internal diffuser area ratio, curvature, and length-to-height ratio. This gap in the information available in the open literature, coupled with the aforementioned experimental results, has directed the authors to look at some simple analytical tools for use in the design of such inlet systems and compare them experimentally to configurations which were designed without benefit of the analysis presented here.

With regard to the direct analysis of inlets and diffusers with a specified geometric configuration, the current state-of-the-art allows the full equations of motion with a sophisticated Reynolds stress tensor model to be applied to the duct. This approach is not, however, an efficient wall contour design technique and generally should be employed to expose the nonideal fluid flow phenomena associated with a family of optimum inlet shapes generated by an inverse method such as the one employed here. To the authors' knowledge, no such calculations utilizing the full equations of motion have been conducted on the generic type of inlet-diffusers considered here. However, some recent experimental studies carried out at NASA Lewis<sup>7</sup> evaluated annular Griffith diffusers whose design was guided by the results of Ref. 8. In this design procedure, the diffuser wall contour is obtained analytically whereas the details of the boundary-layer suction slot region are not emphasized. The results of Ref. 7 indicate a significant improvement in the performance of short annular diffusers with high suction flow rates. On the basis of the studies which are reported here, the detailed contours of the boundary-layer cutoff slot and associated ducting could possibly be optimized to improve diffuser recovery at a smaller suction flow rate. In support of this hypothesis, it has been the authors' experience that, while observing a hot wire

anemometer signal in a boundary layer downstream of a suction slot, the entire character of the flow is extremely sensitive to the inlet *IVR*, lip position, and lip angle for a given overall suction flow rate.

### Analytical Development

The design of a semiflush (i.e.,  $DF > 0$ ) inlet/curved diffuser has been approached in an inverse manner to obtain the resulting physical shape of the bounding surfaces to the flowfield when the surface pressure or velocity distribution is specified. The equations governing the two-dimensional, incompressible, inviscid flow appropriate to this model of the flowfield have been solved over the entire region associated with the inlet, thus resulting in a unified shape which is totally consistent with any local change in the specified surface conditions. The calculation region includes the inlet ramp, curved diffuser, external lip, and the remote streamline which is the lower surface of the computation region shown in Fig. 2.

The governing equations of continuity and irrotationality expressed in spatial Cartesian coordinates and dimensional physical variables are

Continuity

$$\frac{\partial u}{\partial x} + \frac{\partial v}{\partial y} = 0 \quad (1)$$

and

Irrotationality

$$\frac{\partial u}{\partial y} - \frac{\partial v}{\partial x} = 0 \quad (2)$$

The dependent variables can be transformed from the  $x$  and  $y$  components of velocity to the velocity vector magnitude and angle via the following definitions

$$U = \sqrt{u^2 + v^2} \quad (3)$$

and

$$\alpha = \tan^{-1}(v/u) \quad (4)$$

In addition, the independent variables can be transformed from a spatial Cartesian coordinate system to an orthogonal velocity potential-stream function system via the following transformations

$$\frac{\partial \phi}{\partial x} = \frac{\partial \psi}{\partial y} = u \quad (5)$$

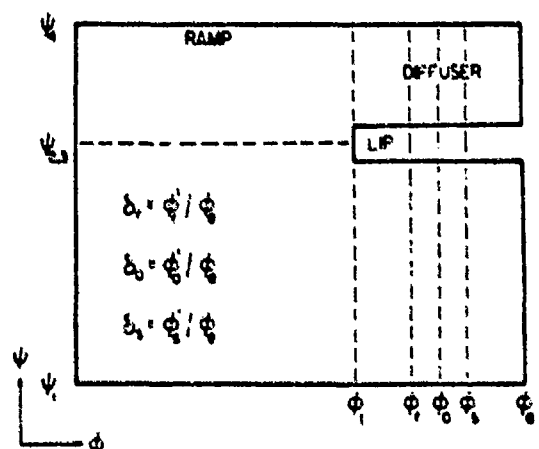


Fig. 2 Mathematical inlet configuration.

and

$$\frac{\partial \phi}{\partial y} = -\frac{\partial \psi}{\partial x} = v \tag{6}$$

Upon applying these transformations to the dependent and independent variables of Eqs. (1) and (2), the governing equations become

Continuity

$$\frac{\partial \ln U}{\partial \phi} + \frac{\partial \alpha}{\partial \psi} = 0 \tag{7}$$

and

Irrotationality

$$\frac{\partial \ln U}{\partial \psi} - \frac{\partial \alpha}{\partial \phi} = 0 \tag{8}$$

By cross differentiating and adding Eqs. (7) and (8), we obtain Laplace's equation for  $\ln U$

$$\nabla_{\phi, \psi}^2 \ln U = 0 \tag{9}$$

After imposing the appropriate boundary conditions on  $\ln U$  in the  $\phi-\psi$  plane, the entire field may be solved (in this paper using successive over-relaxation) for the distribution of  $\ln U$  throughout a grid network appropriate to the inlet geometry as shown in Fig. 2. Once the distribution of  $\ln U$  is known within the field of interest, the physical shape of the bounding surfaces may be obtained from the inverse transformation to Cartesian coordinates. Because of the orthogonality of the  $\phi-\psi$  coordinate system, the inverse transformation can be formed from the following chain rule equations:

$$dx = \frac{\partial x}{\partial \phi} \Big|_{\psi} d\phi + \frac{\partial x}{\partial \psi} \Big|_{\phi} d\psi \tag{10}$$

$$dy = \frac{\partial y}{\partial \phi} \Big|_{\psi} d\phi + \frac{\partial y}{\partial \psi} \Big|_{\phi} d\psi \tag{11}$$

The definitions of the independent variables given in Eqs. (5) and (6) allow us to write

$$d\phi = u dx + v dy \tag{12}$$

and

$$d\psi = -v dx + u dy \tag{13}$$

which can be solved for the appropriate derivatives in Eqs. (10) and (11) resulting in

$$dx = \frac{\cos \alpha}{U} \Big|_{\psi} d\phi - \frac{\sin \alpha}{U} \Big|_{\psi} d\psi \tag{14}$$

and

$$dy = \frac{\sin \alpha}{U} \Big|_{\psi} d\phi + \frac{\cos \alpha}{U} \Big|_{\psi} d\psi \tag{15}$$

These results may now be used to obtain the physical coordinates of each point on any streamline by integrating across  $\phi$  along a constant  $\psi$ . The resulting equation for the  $x$  and  $y$  positions are

$$x_i(\phi) = x_i(\phi_0) + \int_{\phi_0}^{\phi} \left( \frac{\cos \alpha}{U} \right)_{\psi} d\phi \tag{16}$$

and

$$y_i(\phi) = y_i(\phi_0) + \int_{\phi_0}^{\phi} \left( \frac{\sin \alpha}{U} \right)_{\psi} d\phi \tag{17}$$

where the initial coordinates of each streamline are obtained by integrating Eqs. (14) and (15) along the line  $\phi = 0$  from the plane of symmetry streamline to the streamline of interest as shown in the following equations

$$x_i(\phi_0) = - \int_{\phi_0}^{\psi} \left( \frac{\sin \alpha}{U} \right)_{\phi=0} d\psi \tag{18}$$

$$y_i(\phi_0) = \int_{\phi_0}^{\psi} \left( \frac{\cos \alpha}{U} \right)_{\phi=0} d\psi \tag{19}$$

It is now apparent that, to obtain the coordinates of each point on the streamlines of interest, the distribution of  $\alpha$  along those streamlines must be obtained from the known  $\ln U$  field. From the chain rule we can write

$$d\alpha = \frac{\partial \alpha}{\partial \phi} \Big|_{\psi} d\phi + \frac{\partial \alpha}{\partial \psi} \Big|_{\phi} d\psi \tag{20}$$

which, utilizing the conditions of continuity and irrotationality presented in Eqs. (7) and (8), may be rewritten

$$d\alpha = \frac{\partial \ln U}{\partial \psi} \Big|_{\psi} d\phi - \frac{\partial \ln U}{\partial \phi} \Big|_{\psi} d\psi \tag{21}$$

By integrating Eq. (21) along the particular streamlines  $\psi$ , we may determine the distributions of  $\alpha$  necessary to complete the integrations indicated by Eqs. (16-19). Upon performing the indicated  $\alpha$  integration along  $\psi$ , we obtain

$$\alpha_i(\phi) = \alpha_i(\phi_0) + \int_{\phi_0}^{\phi} \left( \frac{\partial \ln U}{\partial \psi} \right)_{\psi} d\phi \tag{22}$$

Here again, the initial streamline angles are obtained by integrating in the  $\psi$  direction along  $\phi = 0$  line from the plane of symmetry streamline to the streamline under consideration. This is done utilizing Eq. (21) and can be written

$$\alpha_i(\phi_0) = - \int_{\phi_0}^{\psi} \left( \frac{\partial \ln U}{\partial \phi} \right)_{\phi=0} d\psi \tag{23}$$

This completes the integrations which must be made utilizing the previously determined  $\ln U$  field, resulting in the specification of the location of each point on the streamlines of interest in physical space.

Inasmuch as the input to the calculation is the surface velocity or pressure on the appropriate boundaries of the calculation region in the  $\phi-\psi$  plane, appropriate distributions

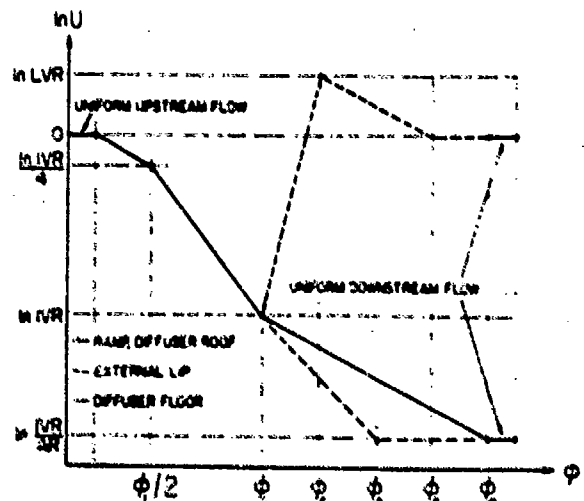


Fig. 3 Inlet surface velocity distribution.

must be selected. For simplicity and ease in manipulating their functional form numerically, velocity profiles of the form  $U \sim e^{-\psi}$  were chosen to form various pieces of the distribution on the respective surfaces of the computation region and are depicted in Fig. 3. Reference 3 points out that one-dimensional flow considerations indicate that velocity distributions of this type are generated by straight wall two-dimensional channels if a one-segment exponential distribution is assumed to exist over the entire length of the channel. On all surfaces of the computation region not noted in Fig. 3, uniform flow may be specified.

The remote streamline was moved sufficiently far from the inlet so as to appear mathematically to be located at infinity. The boundary condition applied at this surface was that of zero normal derivative which forced this streamline to be a plane of symmetry between the inlet flowfield which was calculated and a fictitious mirror image inlet located equidistant beneath the plane of symmetry streamline. The theoretical desirability of having this plane of symmetry available is apparent in the utilization of Eqs. (18, 19, and 23) when we attempt to retrieve the physical shape of the bounding surfaces. In a practical sense, however, the plane of symmetry streamline was located sufficiently far from the inlet so as to have a negligible effect on the resulting inlet shapes, irrespective of the type of boundary condition (i.e., uniform flow or zero normal derivative) which was applied to it.

The effect of smoothing the assumed velocity distribution has been investigated; however, no significant changes in the general inlet shapes were found. Clearly, minor variations in the specific wall shapes ensued; however, no results were found which justified abandoning these straight-line profiles with the corresponding ease of manipulating the various parameters of interest. It is to be emphasized that the choice of this functional form for the boundary conditions is arbitrary and serves only as a reasonable distribution within which the effects of  $I/VR$ , diffuser area ratio, diffuser and ramp length to streamtube height, diffuser curvature, and external lip shape on the resultant inlet configurations can be studied. There is an obvious restriction to the choice of this arbitrary distribution of surface conditions. It arises from the transformation itself which prohibits stagnation points in the flow field. Therefore, the calculated shape of the inlet lip will necessarily be sharp. In actual practice, a parabolic nose will be faired in locally.

### Discussion of the Results

The analysis which has been presented was programmed in double precision and coded in FORTRAN for execution on an IBM 370/168 computer. The computation grid was divided into a  $200 \Delta x \times 150 \Delta y$  rectangular finite-difference mesh which was uniform in each direction. It was determined from numerical experimentation that an optimum position for the

lip streamline occurred at a  $\psi$  value which allowed 25% of the total number of  $\psi$  lines to be located within the inlet streamtube. With the lip streamline located in this position, the solution (obtained through successive over-relaxation) relaxed to its final state in the fewest iterations and was the most accurate (as indicated by the final calculated area ratios of the inlet from its uniform upstream to its uniform downstream) at the maximum iteration limit as shown in Fig. 4. Fixing the lip at a particular  $\psi$  line forced  $\Delta\psi$  to vary from case to case in order that various diffuser configurations might be calculated with different non-dimensional design parameters. Utilizing this uniform rectangular grid whose aspect ratio varied somewhat with the particular inlet being designed, computational times showed some variation. However, a general rule was that, with an over-relaxation parameter of 1.9, the inlet computation would arrive at an asymptotic solution within 400 to 600 iterations utilizing approximately 10 minutes of CPU time.

Once these preliminary setup constraints of the computational procedure were established, the parameters of the inlet surface velocity distributions were systematically varied. Of the parameters available, one was fixed as being a representative value for a desirable inlet shape. This was the quantity which reflected the number of uniform flow grid spaces which were placed upstream and downstream of the inlet. Extensive numerical experimentation established that 25 uniform flow grid spaces provided an adequate inlet shape in that all calculated surfaces were insensitive to further uniform flow additions.

The remaining inlet design parameters were varied in a consistent manner about a nominal inlet configuration to provide a comprehensive picture of how they influenced the resultant inlet shape. These parameters are: area ratio ( $AR$ ), inlet velocity ratio ( $I/VR$ ), external lip velocity ratio ( $LVR$ ), diffuser

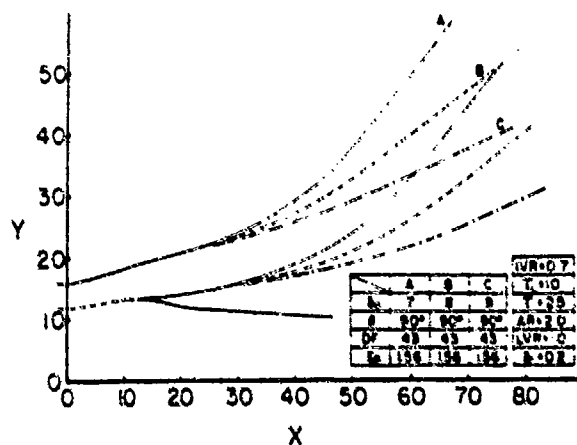


Fig. 5 Effect of  $\delta_0$  on inlet shape.

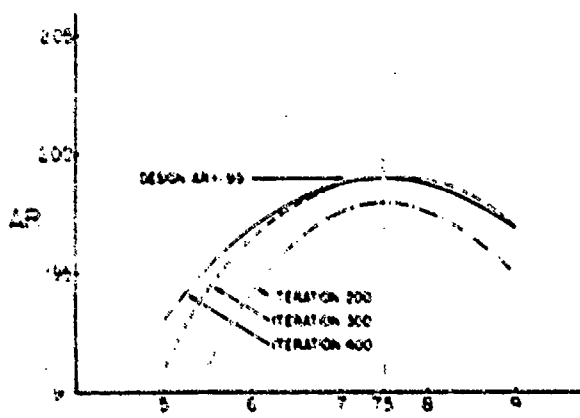


Fig. 4 Effect of lip streamline position on solution convergence.

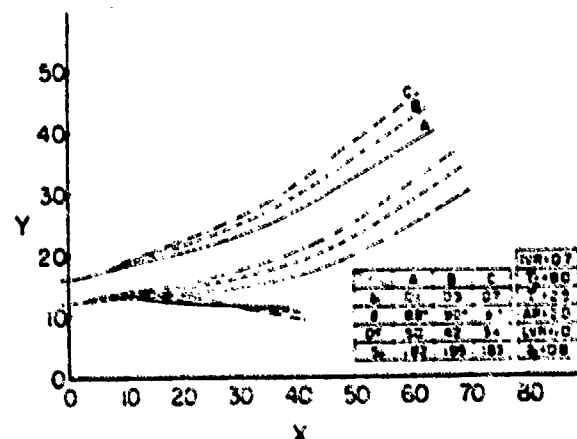


Fig. 6 Effect of  $\delta_0$  on inlet shape.

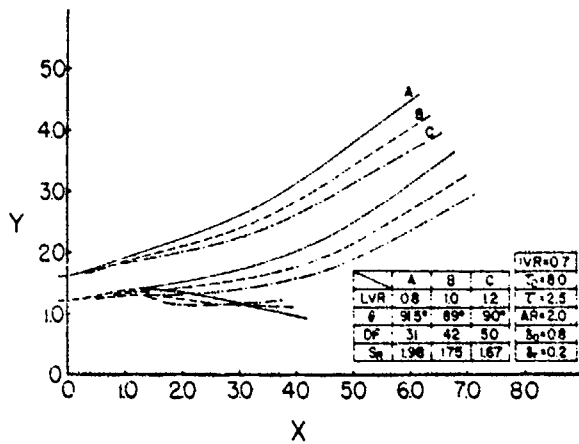


Fig. 7 Effect of  $LVR$  on inlet shape.

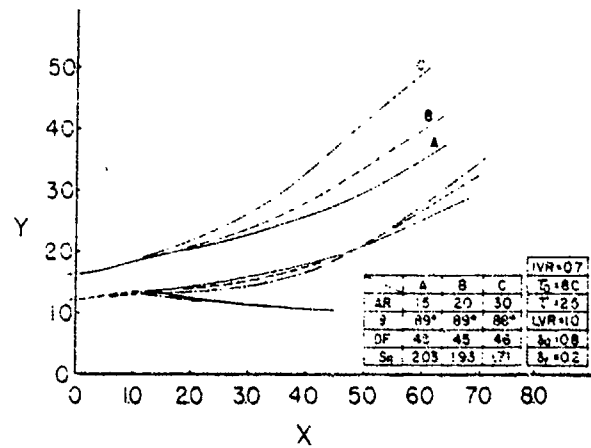


Fig. 9 Effect of  $AR$  on inlet shape.

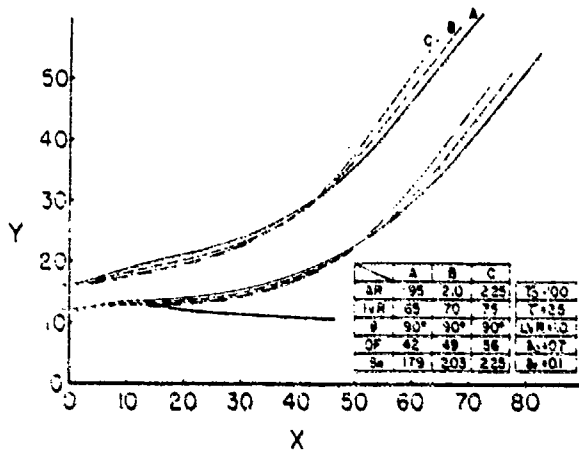


Fig. 8 Effect of  $IVR$  on inlet shape for  $AR/IVR = 3.0$ .

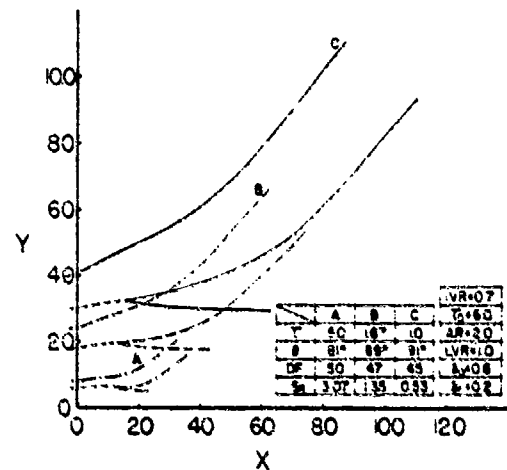


Fig. 10 Effect of  $r$  on inlet shape.

lower surface velocity distribution factor ( $\delta_1$ ), external lip velocity distribution factor ( $\delta_2$ ), diffuser length to height ratio ( $\tau_D$ ), ramp length to streamtube height ratio ( $r$ ), and external lip velocity distribution factor ( $\delta_3$ ) which was held at the constant value of 1.0 after it was determined that  $LVR$  and  $\delta_1$ , exercised sufficient control over the external lip shape. The effect of these parameters on the surface velocity distribution is shown in Figs. 1 and 3. Apart from the basic sensitivity of the inlet shape to these input parameters, secondary inlet characteristics can also be obtained from the calculations. Those inlet characteristics which are an output of the analysis are drop fraction ( $DF$ ), inlet lip angle ( $\theta$ ), and the ramp position ( $S_R$ ) at which the ingested streamtube departs from a line which parallels the ramp, as shown in Fig. 1.

The resultant inlet configurations which are generated when each of the seven principal design variables are varied about a reference state are presented in Figs. 5-10. Although each of the design variables influence all parts of the final inlet shape, for the purpose of general discussion, their principal effects can be separated fairly clearly and general statements as to the characteristics of the inlets controlled by each can be formulated.

The effect of  $\delta_1$ , which controls the diffuser lower surface velocity distribution as shown in Fig. 3, on the inlet shape is primarily the degree to which the diffuser exit curves inboard and directs the flow away from the freestream as shown in Fig. 5. Negligible changes in the lip angle, drop fraction, and ramp shape were observed. However, of primary importance are the relatively flat ramp and the thin lip which allows the flow to diffuse significantly prior to being turned; which are characteristic of all inlets presented here.

Control over the external lip shape is exercised primarily by the parameters  $\delta_2$  and  $LVR$  whose influence on the velocity

distribution is also shown in Fig. 3. The resultant shapes for various values of  $\delta_2$  and  $LVR$  are shown in Figs. 6 and 7 where, apart from the lip shape (which can be changed from concave to convex by a small change in either variable), the principal effect is to lower the diffuser without significant change in the exit angle as the external lip flow acceleration is increased. Changes in the drop fraction are more sensitive to changes in  $LVR$  than they are to changes in  $\delta_2$ , however the general characteristics of a flat ramp in the neighborhood of the inlet lip and a diffuser which attempts to separate turning and diffusion remain intact.

In order to expose the dependence of the inlet shape on  $IVR$ , the total diffusion (i.e.,  $AR/IVR$ ) was held constant at 3.0. The results presented in Fig. 8 illustrate two principal features of these inlets as  $IVR$  and  $AR$  are varied. The first effect which is worthy of note is the sensitivity of lip drop fraction to  $IVR$ , which was also observed on some calculations conducted for a fixed diffuser area ratio as both the  $IVR$  and total diffusion change. The second principal feature of the inlets with varying  $IVR$  is the rapid change in the characteristic shape of the external lip. The results in Fig. 8 indicate this quite clearly when comparing the lip shapes for  $IVR = 0.65$  and  $0.75$ . Because it obscured the figure, the lip for  $IVR = 0.70$  was deleted. In the calculation of inlet shapes with a fixed diffuser area ratio, the effect of  $IVR$  on the external lip shape was even more pronounced than that shown in Fig. 8.

The effect of changing the diffuser area ratio at a constant  $IVR$  is shown in Fig. 9 where a fairly complex change of the diffuser exit angle and diffuser upper surface position are observed. The ramp, external lip, and diffuser lower surface are, however, relatively invariant with  $AR$ .

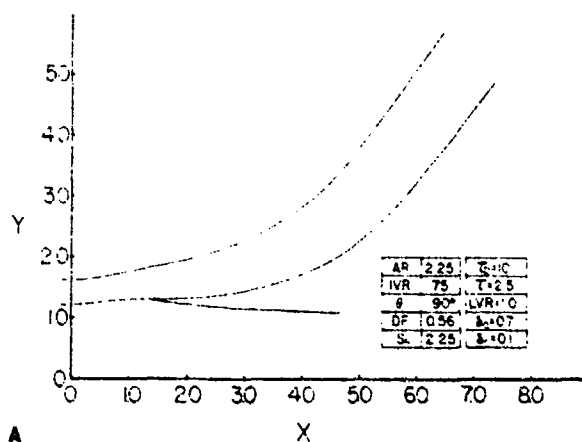


Fig. 11a Representative analytical inlet shape for experimental evaluation; and b) experimental model with sideplate and suction source removed.

Two design control variables whose effect is not shown explicitly on the velocity distributions in Fig. 3 are the diffuser length to inlet height ratio ( $\tau_{01}$ ) and the ramp streamtube length to height ratio ( $\tau$ ). These variables enter the analysis in the transformation from the assumed surface velocity distribution in physical space to the velocity distribution in  $\phi$  and allow the characteristic  $\phi$  values of Fig. 3 to be determined. The influence of an increasing  $\tau_{01}$  on the inlet shape is to a very good approximation simply a stretching of the diffuser around the curvature determined by the diffuser turning parameter ( $\delta_{01}$ ). Some additional effects of secondary importance were slight changes in the lip shape and the extent of the parallel wall, uniform flow region at the diffuser exit.

The results for a varying  $\tau$  are shown in Fig. 10 where the reference length used in the calculations (the length of the ramp to the point where  $\phi = 0$ ) is held constant and the overall inlet decreases in size as the height of the ingested streamtube is varied. The inlet contours presented in Fig. 10 indicate that both the lip angle and the departure points for the ramp streamtube from the ramp are strong functions of the parameter  $\tau$ . These characteristics are even more apparent when the inlets are re-plotted for a constant inlet height with a varying ramp length.

In order to assess the utility of this design method in producing an inlet with adequate pressure recovery capability, a representative inlet configuration (shown in Fig. 11a and 11b) was selected for experimental evaluation. A small, two-dimensional in-draft wind tunnel was built for this purpose. A centrifugal blower was utilized to draw room air through a 10:1 area ratio inlet contraction which contained a series of filters, flow straightening honeycomb and turbulence damping screens. Inlet-diffusers which were tested with the general configuration shown in Fig. 1 were then inverted into the upper surface of the channel. Through active control of

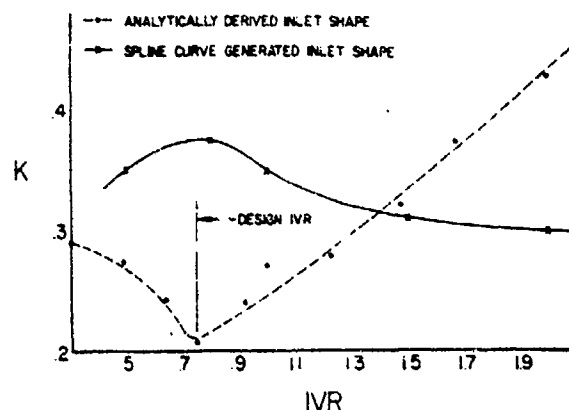


Fig. 12 Experimental inlet loss coefficients.

the surface roughness, the boundary layer approaching the inlet was adjusted to the desired thickness (approximately one-half the inlet height for the test data presented here). Attached to the exit of the inlet/diffuser was a rake of 13 total pressure probes located in the throat of a flow uniformizing venturi immediately downstream of the diffuser exit. Through utilization of the total and static pressure distribution data in the channel downstream of the diffuser exit, the pressure loss and flow rate through the duct were monitored. The magnitude of the flow rate through the inlet was controlled by means of valves located between the diffuser and a second centrifugal blower which was used to draw air from the main-stream flow within the wind tunnel and into the inlet.

The experimental results, presented in Fig. 12, also illustrate the overall inlet loss coefficient  $K$  vs  $IVR$  for an inlet designed by fitting spline curves through the desired inlet and exit positions of the diffuser and lip, which was tested in the same wind tunnel. The data are self-evident in justifying the ability of this method to generate high total pressure recovery inlets. Based on experience with a number of similar inlets in the course of this investigation, it is the authors' belief that lip angle, drop fraction, and diffuser turning expansion distribution are the principal factors affecting the improved total pressure recovery supplied by inlets generated by the analysis presented here.

### Conclusion

Inputting an arbitrary surface velocity or pressure distribution to the inlet design is a particularly desirable task from several standpoints. First, from the point of view of retarding separation as long as possible it may be advantageous to specify the surface pressure distribution so as to avoid peaks in the pressure gradient or to match different experimentally observed pressure distributions which have been determined to delay separation on the ramp, diffuser upper surface, and diffuser lower surface. Second, for use in liquids, the ability to specify the surface pressure distribution is of considerable assistance in controlling the cavitation envelope of the inlet. Third, the consideration of imposing a specific pressure distribution on parts of the inlet to arrive at a favorable force and moment balance can be studied to determine the extent to which it interacts with the separation and cavitation performance. In this case, the unified aspect of this design procedure allows one to study directly the extent to which, for example, changes in the external lip lift force distorts the diffuser or inlet ramp geometry for a given ramp diffuser velocity distribution or forces a distorted ramp-diffuser velocity distribution for a given ramp-diffuser shape. Fourth, when a variable geometry inlet must be designed to operate efficiently at a variety of design points, the inverse method clearly illustrates which surfaces must be movable and in which general direction they must move to allow the inlet to be tuned to its optimum performance in that particular flowfield. Finally, the extent to which certain specified configurations impose unavoidable flow phenomena can be

studied by this method. An example of this involves the semi-flush nature of the inlets presented here. This inlet characteristic is a consequence of the fact that the analysis imposes a uniform flow at the inlet lip by having both the diffuser upper and lower surface velocity profiles originate at  $IVR$  as shown in Fig. 3. It is equally feasible to generate flush inlets by having the diffuser lower surface velocity distribution originate at values somewhat smaller than  $IVR$  and the diffuser upper surface velocity distribution at values somewhat larger than  $IVR$ , thus displacing the inlet lip downstream and more nearly flush. Therefore, we can infer that in a direct attack upon the inlet problem which specifies a flush-type inlet, it might be anticipated that non-uniform inlet velocity profiles could be generated with corresponding diffuser performance problems. This is only one example of the type of feature which a given geometry might impose on the flowfield, a result which becomes clear and casual in this inverse formulation.

#### Acknowledgment

The work presented here was conducted under contract to the U. S. Navy as a part of Contract Number N00024-74-C-0924.

#### References

- <sup>1</sup>Stanitz, J. D., "Design of Two-Dimensional Channels with Prescribed Velocity Distributions Along the Channel Walls," *NACA Report*, 1115, 1953.
- <sup>2</sup>Fox, R. W. and Kline, S. J., "Flow Regimes in Curved Subsonic Diffusers," *Journal of Basic Engineering, Transaction of ASME, Ser. D*, Vol. 84, 1962, pp. 303-316.
- <sup>3</sup>Sagi, C. J., Johnston, J. P., and Kline, S. J., "The Design and Performance of Two-Dimensional Curved Subsonic Diffusers," *Report PD-9*, May 1965, Dept. of Mechanical Engineering.
- <sup>4</sup>Mossman, E. A. and Randall, L. M., "An Experimental Investigation of the Design Variables for NACA Submerged Duct Entrances," *NACA RM A7130*, 1948.
- <sup>5</sup>Hall, C. F. and Barclay, F. D., "An Experimental Investigation of NACA Submerged Inlets at High Subsonic Speeds," *NACA RM A8B16*, 1948.
- <sup>6</sup>Sacks, A. H. and Spreiter, J. R., "Theoretical Investigation of Submerged Inlet at Low Speeds," *NACA TN2323*, 1951.
- <sup>7</sup>Juhasz, A. J., "Effect of Wall Suction on Performance of Short Annular Diffuser at Inlet Mach Numbers Up to 0.5," *NASA TM X3302*, 1975.
- <sup>8</sup>Yang, T., Hudson, W. G., and Nelson, C. D., "Design and Experimental Performance of Short Curved Wall Diffusers with Axial Symmetry Utilizing Slot Suction," *NASA CR2209*, 1973.

# Inverse Design of Optimal Diffusers With Experimental Corroboration

## Gustave Hokenson

Manager of Research,  
Biphase Energy Systems,  
Subsidiary of Research-Cottrell,  
Santa Monica, Calif.  
Mem. ASME

*The equations of motion for a turbulent boundary layer are formulated in an inverse manner and solved to provide the geometrical configuration of optimal two-dimensional diffusers with a distinct inviscid core. For each Reynolds number/diffusion length, optimality is inferred when the lowest exit freestream velocity is computed from the members of an assumed one-parameter family of skin friction decay functions. In addition to the unique inverse formulation and establishment of the appropriate skin friction distribution, an integral part of the analysis is the development of an invertible adverse pressure gradient skin friction law, which is used to solve for the channel-averaged streamwise pressure (inviscid core velocity) distribution. The diffuser configurations are presented graphically for various Reynolds numbers/lengths/blockages and exhibit a distinctive concave shape. The results are compared to three sets of experimental data which support the validity of the viscous flow analysis, the formulation of the governing equations, and the skin friction law which is proposed.*

## Introduction

Theoretical determination of the wall contour, which is required to establish a specified flowfield diffusion and/or turning, is an elegant application of the inverse potential flow theory in [1, 2]. In this approach the surface pressure distribution in the transformed mathematical plane must be input to the analysis. The solution and subsequent retransformation to the physical plane provides the desired duct configuration. In order to specify a meaningful surface pressure distribution, however, the boundary layer behavior must be considered.

In recent years, turbulence modeling methodology (see [3]) has been elevated to the point where equations which represent the entire Reynolds stress tensor may be applied to compute the flow through any specified channel. Additionally, available experimental data [4] on diffuser performance is coming under control with the proper treatment of boundary layer effects. With such correlated data, the general configuration of optimal diffusers may be inferred. Ideally, the most accurate analytical models should be utilized to compute the detailed diffuser geometry. Complexities in such an analytical formulation and its computational magnitude have, to this point, prohibited such an approach. In fact, few analyses are available which provide a wholly rational diffuser design and those which seek out the optimum configurations are rare.

Generally, an unseparated flow condition with maximum static pressure recovery in the diffuser is sought. The displacement thickness distribution is computed to correct the

indicated potential flow wall contour for boundary layer blockage effects. In the direct problem this procedure is iterative (not necessarily convergent) and provides no straightforward mechanism for establishing an optimal diffuser contour.

To fill this void, a new diffuser design technique has been developed which utilizes an original algebraic skin friction model based on data correlations for flows in adverse pressure gradients. The conventional boundary layer equations are combined with this skin friction model in an inverse manner and optimality is established by maximizing the diffuser pressure recovery with respect to a single parameter which characterizes the skin friction distribution along the diffuser. The governing equations then provide simultaneously the boundary layer thickness and freestream velocity distribution, from which the optimal diffuser configuration may be inferred from either one-dimensional or inverse potential flow.

In conjunction with available experimental data, the analysis establishes a rational diffuser design methodology, affirms the validity of a new skin friction correlation, defines the characteristic optimal skin friction decay, and generates conceptually new diffuser wall contours for experimental evaluation.

## Analysis

Since an unseparated diffuser is sought, the skin friction should vary from its constant pressure value near the diffuser entrance to a small value at the exit. The optimal path between these two extremes is that which provides the lowest inviscid core velocity at the diffuser exit (i.e., maximum static pressure recovery). In order to restrict the mathematical scope of the problem, the optimization process is simplified by specifying the skin friction decay function to be a one

Contributed by the Fluids Engineering Division of The American Society of Mechanical Engineers and presented at the Winter Annual Meeting, New York, N.Y., December 2-7, 1979. Manuscript received at ASME Headquarters January 10, 1979. Paper No. 79-WA/FE-13.

parameter family which approaches zero with a zero derivative at the diffuser exit. This exit condition enhances the possibility of establishing an equilibrium incipiently separated flow as in [5], but excludes cases of increased recovery with slight stall in [6] which have their origin in explicit transient flow phenomena.

Such a one parameter family with the requisite boundary conditions is given by the equation.

$$\bar{C}_f = (1 - \bar{x})^N \quad (1)$$

By assuming a distribution of values for  $N (\geq 1)$  for each flowfield studied, the equations of motion may be solved to determine *simultaneously* the corresponding distributions of  $\delta^*$  and  $U$  along the channel. The  $N$  value which provides the minimum freestream velocity at the channel exit is taken to be that which characterizes the optimal skin friction decay. It will become apparent that the optimal  $N$  is not infinitely large, and this fact can be attributed primarily to the shape factor growth as separation is approached.

Clearly, the assumed skin friction distribution must be input to the equations of motion which are utilized here in the following integral form:

$$\bar{\theta}(x) - \bar{\theta}_i = \int_0^x (\bar{C}_f C_f / 2 - \bar{S}(H+2)S_{cr}) dx \quad (2)$$

Note that the pressure gradient term is included in the integrand on the right-hand side of equation (2) due to the inverse nature of the computational procedure, as discussed in the next section. Additionally, expressions for  $H$  (in terms of  $H_0$ ,  $H_{cr}$ , and  $\bar{S}$ ) and  $\bar{S}$  (in terms of  $\bar{C}_f$ ) must be developed. The nonlinear interpolation formula developed in [7] for  $H$  was utilized, with values for  $H_0$ ,  $h_c$ , and  $S_{cr}$  as functions of Reynolds number taken from [7] through [13], along with the  $C_f$  correlation. By correlating the data from [7], the following adverse pressure gradient skin friction law, which forms the basis for all the analytical results that follow, is obtained:

$$\bar{C}_f = \frac{1 - \bar{S}}{1 + \alpha \bar{S}}$$

or:

$$\bar{S} = \frac{1 - \bar{C}_f}{1 + \alpha \bar{C}_f} \quad (3)$$

where:

$$\alpha = \frac{1 - 2g(\text{Re}_{ii})}{g^2(\text{Re}_{ii})} \quad (4)$$

and:

$$g(\text{Re}_{ii}) = 0.702 - 0.108 (\log_{10} \text{Re}_{ii}) + 6.16 \times 10^{-3} (\log_{10} \text{Re}_{ii})^2 \quad (5)$$

The (enforced) asymptote for  $\phi$  is 10.22 at  $\text{Re}_{ii} = 5.76 \times 10^8$ , which is the high Reynolds number (limiting flow) value appropriate to the developments in [7].

Future work utilizing algebraic skin friction correlations which contain explicit effects due to turbulent flow history and wall curvature should increase the universality of this analytical approach.

### Method of Solution

In order to integrate equation (2) with conventional quadrature algorithms, the characteristic flowfield parameters  $\text{Re}_{ii}$  and  $L/\theta_i$  must be specified, allowing the constant of integration ( $\bar{\theta}_i$ ) and  $C_f$  to be determined. Additionally, equation (1) provides  $\bar{C}_f$  once  $N$  is specified. The heart of the computation, however, lies in utilizing equation (3) to supply  $\bar{S}$  in equation (2), in terms of the known  $\bar{C}_f$ . With this mating of equations (1) through (3) and the functional formulation for  $H$ , equation (2) may be integrated utilizing expressions for  $C_{fo}$ ,  $H_0$ ,  $H_{cr}$  and  $S_{cr}$  in terms of the local Reynolds number ( $\text{Re}_{ii}$ ). In order to determine the local Reynolds number, the local freestream velocity must be known and is obtained from the concurrent integration of equation (3), utilizing the aforementioned functional inputs. The freestream velocity is also required to establish the diffuser geometry based on an inviscid flow analysis.

From equations (1) and (3), and the definition of  $\bar{S}$ , it is apparent that rapid growth of  $\bar{\theta}$  is detrimental to obtaining large freestream velocity decelerations. The optimal  $\bar{\theta}$  growth is a trade-off between the rate at which  $\bar{S}$  approaches one (i.e.,  $C_f \rightarrow 0$ ) in equations (2) and (3), and the rate at which  $H$  increases to  $H_{cr}$  in equation (2). Therefore, an optimal, finite value of  $N$  is to be expected.

In summary, after specifying  $\text{Re}_{ii}$  and  $L/\theta_i$ , the solution of the governing equations provides the distributions of  $\bar{C}_f$ ,  $\bar{\theta}$ , and  $H$  for a given  $N$ . Upon solving for  $\bar{U}_i$  as a function of  $N$  at a given  $\text{Re}_{ii} - L/\theta_i$  combination, the optimal diffusion (for this particular one parameter family of skin friction decay functions) may be identified. In order to display the geometric configuration of these optimal diffusers,  $\bar{U}$  is assumed to be uniform across the inviscid core and the one-dimensional continuity equation is applied to a two-dimensional diffuser (divergence in one plane) resulting in:

$$(w/L)/(h_c/L) = \bar{U}^{-1} + B \delta^* \quad (6)$$

where the physical interpretation of displacement thickness has been utilized. In addition, the effective inviscid core height at the inlet has been utilized as a characteristic length

<sup>1</sup>Asymmetric diffuser configurations may be established for small displacements only, inasmuch as the governing equations do not fully account for transverse curvature effects, as discussed in [14].

### Nomenclature

$AR$  = area ratio  
 $B$  =  $(\delta^*/h)$   
 $B'$  =  $(\delta^*/h)$   
 $C_f$  = skin friction coefficient  
 $\bar{C}_f$  =  $C_f/C_{fo}$   
 $\bar{C}_f$  =  $C_f/C_{fo}$   
 $C_r$  = diffuser static pressure recovery coefficient  
 $g$  = function of  $\text{Re}_{ii}$  in equation (5)  
 $H$  = shape factor,  $\delta^*/\delta$   
 $h$  = effective inviscid core half-height

$L$  = streamwise wetted length  
 $N$  = exponent in equation (1)  
 $\text{Re}_{ii}$  = Reynolds number  
 $\bar{S}$  =  $h/d$  ( $\bar{C}_f/2$ )  
 $\bar{S}$  =  $S/S_{cr}$   
 $U$  = freestream velocity  
 $\bar{U}$  =  $U/U_i$   
 $u$  = channel half-height  
 $x$  = streamwise coordinate  
 $\bar{x}$  =  $x/L$   
 $\delta^*$  = displacement thickness  
 $\delta$  =  $\delta^*/\delta^*$

$\theta$  = momentum thickness  
 $\bar{\theta}$  =  $\theta/\theta_i$   
 $\phi$  = function of  $g$  in equation (4)

### Subscripts

$cr$  = conditions at separation  
 $f$  = conditions at diffuser exit  
 $i$  = conditions at diffuser inlet  
 $o$  = constant pressure  
 $\theta$  = referenced to  $\theta$   
 $L$  = referenced to upstream wetted length

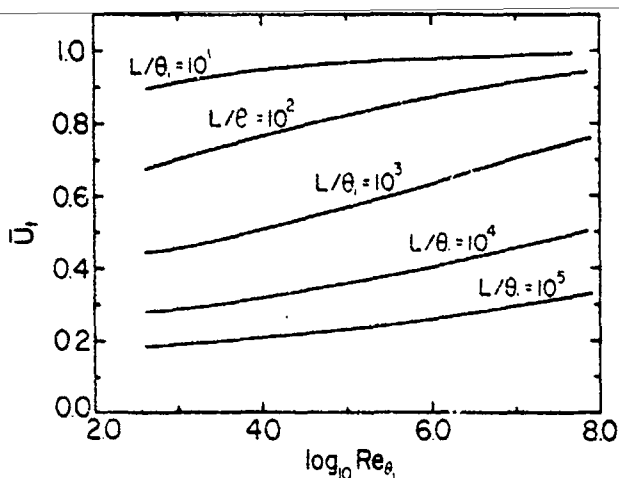


Fig. 1  $U_i$  versus  $Re_{\theta_1}$  for various  $L/\theta_1$

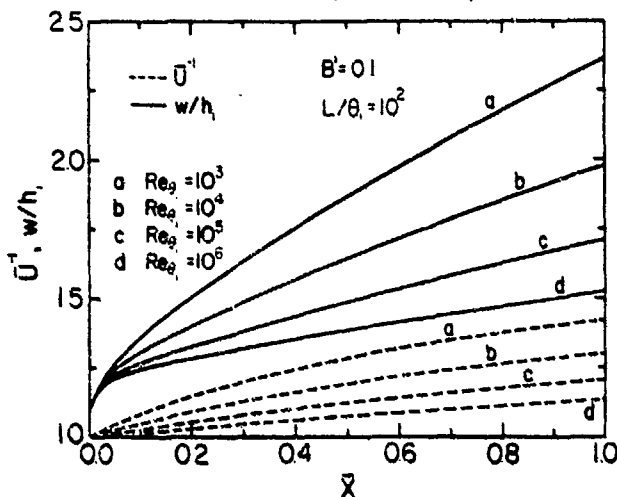


Fig. 2 Diffuser wall and inviscid core area distribution for  $Re_{\theta_1} = 10^3 - 10^6$  at  $L/\theta_1 = 10^2$  and  $B' = 0.1$ ,  $L/2W_1 = 3.48, 3.82, 3.74, 3.83$

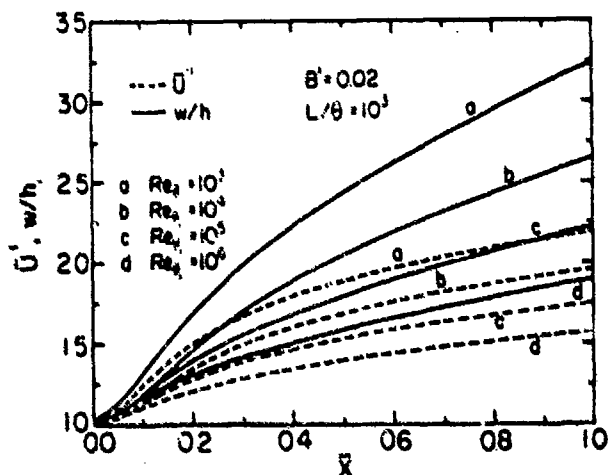


Fig. 3 Diffuser wall and inviscid core area distribution for  $Re_{\theta_1} = 10^3 - 10^6$  at  $L/\theta_1 = 10^3$  and  $B' = 0.02$ ,  $L/2W_1 = 7.47, 7.81, 8.08, 8.28$

( $B' = (\delta^*/h)$ ), in lieu of the total channel height, to obtain a concise functional form with linear dependence upon a single boundary layer parameter. The conventional boundary layer blockage ( $B = (\delta^*/w)$ ) is related to  $B'$  by  $B = B'/(1 + B')$ . By specifying the diffuser blockage, or inviscid core aspect ratio ( $L/h_c$ ) which are related by  $L/h_c = (L/\theta_1)(B'/H_1(Re_{\theta_1}))$ , equation (6) was evaluated with the solutions of the equations of motion to provide the channel

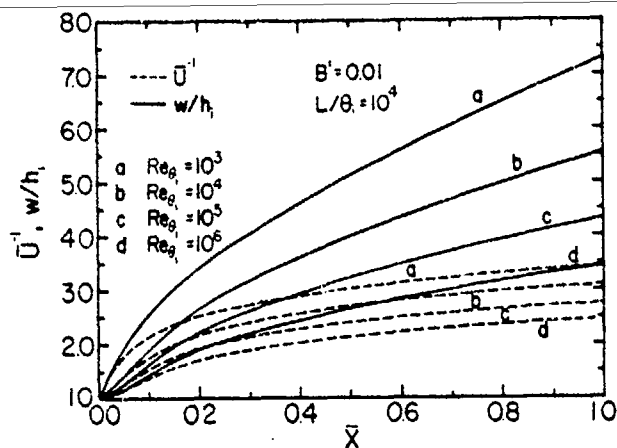


Fig. 4 Diffuser wall and inviscid core area distribution for  $Re_{\theta_1} = 10^3 - 10^6$  at  $L/\theta_1 = 10^4$  and  $B' = 0.01$ ,  $L/2W_1 = 37.70, 39.41, 40.71, 41.71$

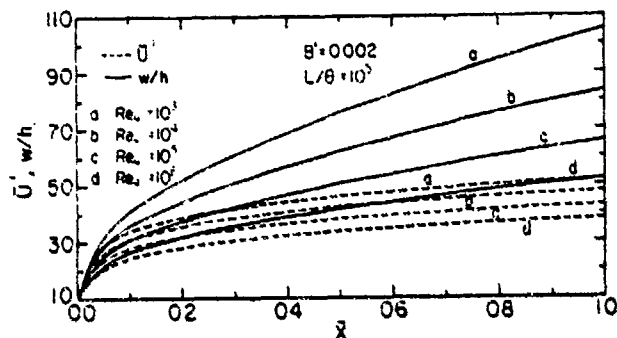


Fig. 5 Diffuser wall and inviscid core area distribution for  $Re_{\theta_1} = 10^3 - 10^6$  at  $L/\theta_1 = 10^5$  and  $B' = 0.002$ ,  $L/2W_1 = 76.01, 78.48, 82.07, 84.08$

geometry. The inviscid core aspect ratio is related to the conventional diffuser aspect ratio ( $L/2W_1$ ) by  $L/2W_1 = (L/h_c)/(1 + B')^{1/2} = (L/h_c)/(1 - B)/2$ . Note that other commonly used variables, such as duct Reynolds number, are simple functions of the parameters utilized here to characterize the flowfield.

When the diffuser geometries are presented graphically, the  $B' = 0$  curve is plotted to represent the effective inviscid core area distribution. A second curve, which is the (assumed) inviscid core added to a linearly scaled and normalized displacement thickness distribution, is plotted to represent the (two-dimensional) diffuser wall. Therefore, with this boundary layer blockage representation, the displacement thickness growth is readily observed and revealed for different flowfield conditions.

Clearly, the computed pressure gradient could be established without a distinct inviscid structure and the resultant diffuser area gradients/divergence angles would be smaller. In such computations, it is more relevant to associate the definition of  $\delta$  directly with the pressure gradient and utilize the channel-averaged momentum and continuity equations to provide the cross-sectional area distribution for any geometric class of diffusers.

In either case, the one-dimensional flow assumption carries the inherent approximation of neglecting flow non-uniformities across the diffuser due to wall curvature. This effect shall be assessed in future research utilizing inverse potential flow analysis [1, 2] to generate the wall contour.

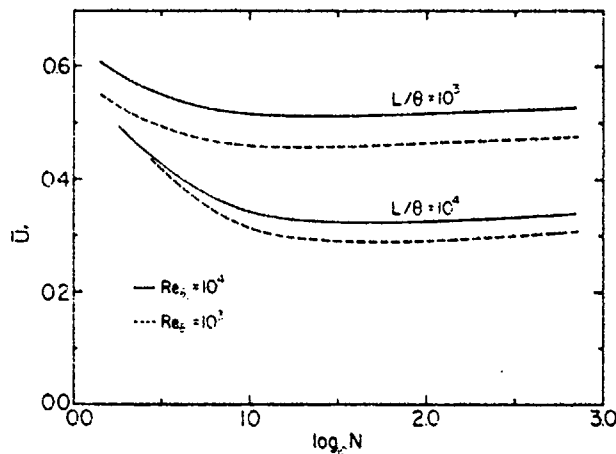


Fig. 6.  $U_1$  versus  $N$  for various  $L/\theta_1$  and  $Re_{\theta_1}$

### Analytical Results

For Reynolds numbers from  $Re_{\theta_1} = 10^3 - 10^6$  and diffusion lengths from  $L/\theta_1 = 10^1 - 10^5$ , the governing equations were solved numerically utilizing a distribution of values for  $N$  sufficient to determine the optimal skin friction decay in each situation. The velocity ratio across the diffuser (for the optimal  $N$ ) has been plotted versus  $Re_{\theta_1}$ , with  $L/\theta_1$  as a parameter in Fig. 1. For a given diffuser length and inlet Reynolds number, reducing the diffuser entrance momentum thickness is a process which moves diagonally across the figure toward the lower left hand corner.

The diffuser geometries corresponding to the decelerations indicated in Fig. 1 are presented in Figs. 2 through 5 for  $L/\theta_1 = 10^2 - 10^5$  and  $Re_{\theta_1} = 10^3 - 10^6$  which encompasses the configurations of primary interest. Note that each relative length configuration is associated with a specified blockage factor ( $B'$ ), which was selected for clarity of data presentation. The corresponding aspect ratios (as indicated on the figure caption) are not necessarily always physically realistic and the data may be re-scaled to any desired blockage.

Of particular interest is the fact that the diffusers which have been computed assume a characteristic concave shape (when viewing the flow side, excepting the immediate entrance) so as to retard the thin upstream boundary layers more strongly than the downstream flow. This is an extension of the logical deceleration mechanism which has been set forth in proposing and rationalizing the performance of straight-wall diffusers. The unique diffuser configuration at the entrance plane is a result of the lag between constant pressure initial conditions and the establishment of a boundary layer growth in response to strong adverse pressure gradients. Experimentally observed conditions [5] at the immediate entrance to the diffuser are also associated with the transition of the pressure field from constant to increasing pressure.

The sensitivity of the results to  $N$  in the neighborhood of its optimum value may be seen in the data of Fig. 6. Clearly, the boundary layer growth is sensitive to the pressure gradient but, utilizing the inverse formulation, the optimal pressure gradient is not sensitive to  $N$  in the neighborhood of the optimum  $N$ . Therefore, the results presented here should not be unduly restrictive due to the choice of equation (1).

### Experimental Comparisons and Conclusions

The analytical results presented here provide a graphic indication of the degree to which boundary layer control allows even large area ratio diffusers to perform efficiently. Consider the dramatic results from [15] in which the static pressure recovery efficiency for a 4:1 area ratio diffuser varies from 0.70 at  $B = 0.06$  to approximately 0.97 with uniform entrance flows (inferred by extrapolation). Maintaining a

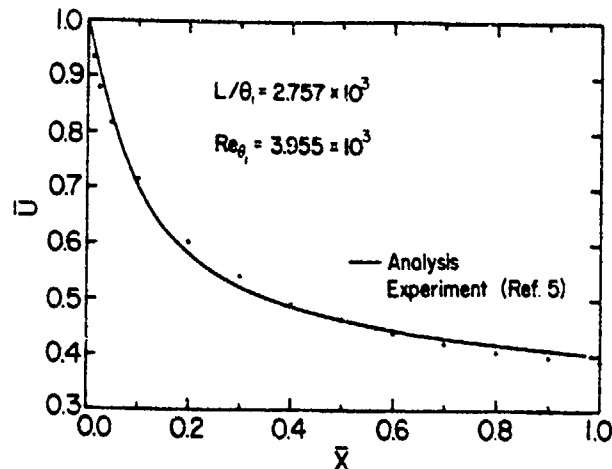


Fig. 7 Comparison of analytical and experimental velocity distributions at  $L/\theta_1 = 2.757 \times 10^3$  and  $Re_{\theta_1} = 3.955 \times 10^3$

turbulent entrance boundary layer and an incompressible flow, the diffusion length for these blockages covers the range  $L/\theta_1 = 5 \times 10^2 - 10^5$  at a Reynolds number of  $10^3$ . The results of the computations carried out here indicate that the efficiency of an optimal 7.15:1 aspect ratio ( $L/2W_1$ ) diffuser (as used in [15]) increases from 0.75 to 0.99 over this variation in  $L/\theta_1$ , as the entrance momentum thickness essentially approaches zero. This corroboration supports the position that very large optimal decelerations predicted theoretically are experimentally achievable for sufficiently thin diffuser entrance boundary layers.

The extensively quoted data of [16] provide a further test of the analytical results obtained here. For a blockage factor ( $B$ ) of 0.03 and an aspect ratio ( $L/2W_1$ ) of 18.0, the experimental results in Fig. 10 [16] indicate an optimum  $C_p$  of 0.73 at an area ratio of 3.0 which leads to an efficiency of 0.82. The value of  $Re_{\theta_1}$  appropriate to the experiment in [13] is approximately  $1.5 \times 10^3$  with a corresponding  $L/\theta_1 = 1.8 \times 10^3$ . If the data obtained here at  $Re_{\theta_1} = 10^3$  and  $L/\theta_1 = 10^3$  is utilized, the optimum diffuser is indicated at an area ratio of 3.25 with an efficiency of 0.82. The theoretical results are, therefore, reasonable predictions of the actual diffuser performance and reinforce the experimental indications from [16] of a potential benefit from contouring the skin friction decay and resultant diffuser cross-sectional area distribution.

A large portion of the experimental studies on diffusers reported in the open literature lies in the regime  $L/\theta_1 = 10^3 - 10^4$  and  $Re_{\theta_1} = 10^3 - 10^4$ . The optimal two-dimensional diffusers which have been plotted look "familiar" for the relatively larger  $\theta_1$  values in this range. In fact, as has been shown, the analytically computed diffuser performance closely follows available experimental results. It is apparent that, as the design point for the diffuser penetrates the low  $Re_{\theta_1}$  - high  $L/\theta_1$  corner of the analysis, the configurations depart from those commonly accepted for optimal diffusers. Therefore, the excellent NBS data from [5] has been used to validate the analysis for large diffusion lengths and freestream velocity decelerations, inasmuch as it forges further into the clean entrance domain with essentially two-dimensional flow. That experimental work was also directed at establishing an incipiently separating, yet stable, boundary layer flow which is relevant to the class of optimal diffusers presented here.

From the wind tunnel turbulence damping screen to the streamwise position where (in Fig. 3 of [5]) the adverse pressure gradient takes hold is approximately 1.457 m. Based on the conditions quoted in [5], the resultant value of  $\theta_1$ , relevant to the analysis employed here is 2.881 mm, which was obtained from the flat plate turbulent boundary layer growth "law":  $\theta_1/L_1 = 0.036/Re_{\theta_1}^{0.2}$ . This agrees with the ex-

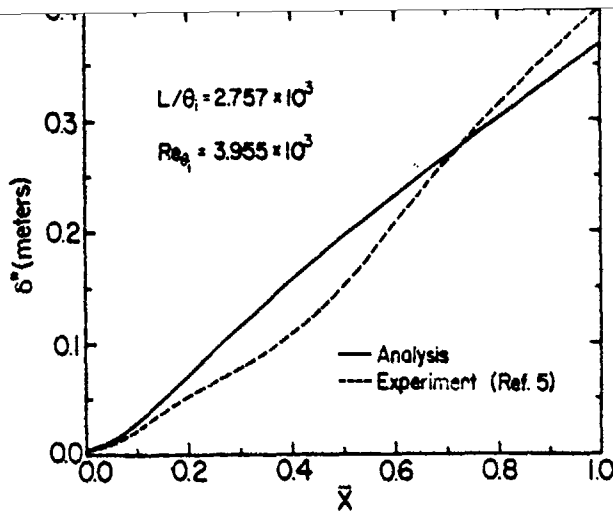


Fig. 8 Comparison of analytical and experimental displacement thickness distributions at  $L/\theta_1 = 2.757 \times 10^3$  and  $Re_{\theta_1} = 3.955 \times 10^3$

perimental results in Fig. 8, [5] and establishes a corresponding diffuser entrance Reynolds number of  $Re_{\theta_1} = 3.955 \times 10^3$ .

With the exception of the transition from constant pressure to an adverse pressure gradient, the skin friction coefficient profile from Fig. 5 [5] is similar to the decay function which was utilized here. It is to be remembered that the dependence of  $\bar{U}_f$  (and the resultant streamwise profile) on  $N$  is relatively weak in the neighborhood of the optimum  $N$ . Therefore, the experimental reality is that the skin friction decay in [5] which establishes incipient separation may be optimal.

The results in Fig. 5 [5] indicate that the point of zero skin friction would occur at approximately 8.13 m. This implies an  $L/\theta_1 = 2.757 \times 10^3$  after accounting for the 0.187-m transition section between the uniform velocity and power law velocity decay regions. Utilizing an  $Re_{\theta_1} = 3.955 \times 10^3$  and  $L/\theta_1 = 2.757 \times 10^3$ , the data from Fig. 1 may be entered with a non-linear interpolation scheme which provides a value for  $\bar{U}_f = 0.29 \pm 0.01$ . The results of Fig. 3 [5] may be extrapolated to 8.13 m, indicating a  $\bar{U}_f = 0.38 \pm 0.02$ . In fact, the entire freestream velocity and displacement thickness distributions predicted by analysis, shown in Figs. 7 and 8, compare favorably with that which [5] presents as characteristic of incipient separation.

In summary, the analytical results obtained here are substantiated by experimental data for flows in adverse pressure gradients which approach separation and, therefore,

the validity of equations (1) and (3) and the overall theoretical viscous flow approach is confirmed. The geometrical configuration of the diffusers obtained from quasi-one-dimensional flow analysis points to the need for a critical assessment of diffuser contouring (as in [16]) and its interaction with the incoming boundary layer. In addition, the examination of large diffusion in the presence of very clean entrance conditions ( $B \sim 0(10^{-4})$ ) through use of efficiently designed boundary layer cut-off slots [2] is indicated.

## References

- 1 Stanitz, J. D., "Design of Two-Dimensional Channels with Prescribed Velocity Distributions Along the Channel Walls," NACA Report 1115, 1953.
- 2 Hokenson, G. J. and Su, F. Y., "Unified Inlet/Diffuser Design by an Inverse Method," *AIAA Journal*, Vol. 15, No. 1, Jan. 1976, pp. 39-45.
- 3 Reynolds, W. C., "Computation of Turbulent Flows," *Annual Review of Fluid Mechanics*, Vol. 8, 1976, pp. 183-208.
- 4 Sovran, G. and Klomp, E. D., "Experimentally Determined Optimum Geometries for Rectilinear Diffusers with Rectangular, Conical or Annular Cross-Section," *Fluid Mechanics of Internal Flow*, ed. Gino Sovran, Elsevier, New York, 1967, pp. 270-319.
- 5 Spangenburg, W. G., Rowland, W. R., and Mease, N. E., "Measurements in a Turbulent Boundary Layer Maintained in a Nearly Separated Condition," *Fluid Mechanics of Internal Flow*, ed. Gino Sovran, Elsevier, New York, 1967, pp. 110-151.
- 6 Ghose, S. and Kline S. J., "Prediction of Transitory Stall in Two-Dimensional Diffusers," Report MD-36, Thermosciences Division, Dept. of Mechanical Engineering, Stanford University, Dec. 1976.
- 7 Kutateladze, S. S. and Leont'ev, A. I., *Turbulent Boundary Layers in Compressible Gases*, Trans. by D. B. Spalding, Academic Press, New York, 1964.
- 8 Schubauer, G. B. and Klebanoff, P. S., "Investigation of Separation of the Turbulent Boundary Layer," NACA Report 1030, 1951.
- 9 Von Doenhoff, A. E. and Tetervin, N., "Determination of General Relations for the Behavior of Turbulent Boundary Layers," NACA Report 772, 1943.
- 10 Newman, B. G., "Some Contributions to the Study of the Turbulent Boundary Layer Near Separation," ARC ARL Report ACA-53, 1951, Melbourne, Australia.
- 11 Nikuradse, J., "Untersuchungen über die Strömungen des Wassers in konvergenten und divergenten Kanälen," *Forschungsarbeiten of the VDI*, No. 289, 1929.
- 12 Buri, A., "Eine Berechnungsgrundlage für die turbulente Grenzschicht bei beschleunigter und verzögerter Strömung," Dissertation, Zurich, 1931.
- 13 Schlichting, H., *Boundary Layer Theory*, trans. by J. Keestin, 6th ed., McGraw-Hill, New York, 1968.
- 14 Hokenson, G. J., "Consistent Integral Thickness Utilization for Boundary Layers with Transverse Curvature," *AIAA Journal*, Vol. 15, No. 4, April 1977, pp. 597-600.
- 15 Ackeret, J., "Grenzschichten in geraden und gekrümmten Diffusoren," IUTAM-Symposium Freiburg BR, 1957, ed. by H. Görtler, 1958, Berlin, pp. 22-37.
- 16 Carlton, I. J. and Johnston, J. P., "Effects of Wall Shape on Flow Regimes and Performance in Straight, Two-Dimensional Diffusers," Rept. PD-11, June 1965, Thermosciences Div., Dept. of Mech. Engr., Stanford University.

# Optimal Two-Phase-Flow Nozzle Configurations at Large Volume Ratios

Gustave Hokenson\*  
Dynamics Technology, Inc., Torrance, Calif.

A self-consistent methodology for establishing the optimal geometric configuration of two-phase-flow converging-diverging nozzles is developed. The analysis relies on a perturbation of the isentropic, homogeneous, equilibrium (IHE) flow model to establish the area ratio, contour, and length scale of optimally efficient nozzles in the limit of large volume ratios. The IHE limit model predicts the pressure-area relationships with reasonable accuracy and provides a simple analytical representation of the bulk flowfield. This formulation is used in the determination of a nozzle contour which minimizes wall friction losses and an aspect ratio which optimizes the nozzle length in a tradeoff between phase slip and wall friction. These optimization procedures are coupled and applied iteratively, result in a nozzle configuration which optimally accommodates the effects of wall shear, interphase drag, and pressure gradients. Comparison with experimental data is used to validate the approach within the context of the assumptions which were enforced.

## Nomenclature

$a$	= speed of sound
$A$	= cross-sectional area
$c$	= constant in Eq. (7) for $\delta$
$C_D$	= particle drag coefficient
$C_f$	= skin friction coefficient
$D_0$	= particle scale
$D_N$	= hydraulic diameter
$E$	= Euler number, $\rho/\rho_0 u^2$
$f, g, h, j$	= functions defined in Eq. (7)
$J$	= generalized integrand
$k_1$	= constant in Eq. (8), $2C_f(L/D_N)$
$k_2$	= constant in Eq. (8), $3C_D(L/D_0)/4$
$L$	= nozzle length
$M$	= Mach number
$p$	= pressure
$r$	= ratio of liquid to gas mass flow rate
$S$	= nozzle surface area per unit length
$u$	= velocity
$u_r$	= relative velocity, $u_g - u_l$
$\bar{u}$	= bulk velocity
$v$	= volume ratio, $(\rho_l/\rho_g)/r$
$We$	= Weber number, $\rho u^2 D_0/\sigma$
$x$	= streamwise position
$\beta$	= $M^2 - 1$
$\delta, \epsilon$	= parameters defined by Eq. (7)
$\lambda_1$	= $(u_l/u_g)^*$
$\lambda_2$	= $(\rho_l u_l^2/\rho_g u_g^2)^*$
$\lambda_3$	= $(p/\rho u^2)^*$
$\rho$	= density
$\sigma$	= surface tension
$\theta$	= momentum thickness
$\eta$	= efficiency, $(\bar{u}_e/\bar{u}_{opt})^2$

## Subscripts

crit	= conditions for particle breakup
e	= nozzle exit
g	= gaseous
l	= liquid

0	= initial or reference conditions
$t$	= stagnation conditions

## Superscripts

$( )^*$	= critical or throat conditions
$(-)$	= normalized by throat conditions or $L$
$( ' )$	= differentiation with respect to $x$

## Introduction

COMPLICATIONS introduced by multiphase flow to the design of efficient converging-diverging nozzles are significant.<sup>1,2</sup> Optimal length scaling (aspect ratio), contouring, and area ratio are sensitive to the detailed bubble growth/particle breakup and dynamics. As discussed in Ref. 3, these phenomena are often complex and not easily modeled. This restricts the utility of large-scale computational algorithms whose design predictions are difficult to distill into a compact form. Therefore, an approximate solution which perturbs the isentropic, homogeneous, equilibrium (IHE) flow model was developed to synthesize the optimal nozzle geometry for anisentropic, nonhomogeneous, nonequilibrium situations.

## Area Ratio

In the limit of large volume ratio ( $v$ ), and assuming that the density ratio is sufficiently small for the mass ratio to be  $> 1$ , the IHE model of two-phase flow (see Ref. 4) may be expanded to provide the following approximate relationships:

$$\frac{\rho_l u^2/2}{p_t} = v, \ln(p_t/p) \quad (1)$$

and

$$\frac{\rho_l u^2/2}{p_t} = v, 1/2 \quad (2)$$

Applying Eq. (1) at the nozzle throat and substituting for  $a$  from Eq. (2) results in

$$p^*/p_t = p^*/p_0 = e^{-v} \quad (3)$$

Combining Eqs. (1) and (2), the local Mach number may be written

$$M^2 = \ln(p_t/p)^2 \quad (4)$$

Received Dec. 30, 1980; revision received June 25, 1981. Copyright © American Institute of Aeronautics and Astronautics, Inc., 1981. All rights reserved.

\*Senior Research Scientist, Member AIAA.

Utilizing continuity of mass flow, the local area ratio becomes

$$\bar{A}^2 = e^\beta / (1 + \beta) \quad (5)$$

where  $\beta = \ln(p_1/p) - 1$  and, therefore, from Eq. (4)  $\beta = M^2 - 1$ .

The validity of these formulas may be evaluated by comparison with the results in Refs. 1 and 2 for air/water nozzles operating at  $r = 10$  and  $p_1/p_e = 35$ . Equation (5) predicts full expansion at  $\bar{A}_e = 7.96$ , whereas the (suboptimal) pressure contour design analysis in Ref. 2 results in  $\bar{A}_e = 7.022$ . Evaluation mode results were computed in Ref. 1 for identical conditions in an annular nozzle with an approximately linear area distribution in the supersonic region. These computations indicate that sensible expansion ceases at  $\bar{A} = 6.93$  for both 7 and 21 deg divergence angle nozzles. Equation (3) satisfactorily predicts the throat conditions for both sets of data.

This simple IHE limit model provides the framework within which anisentropic, nonhomogeneous, nonequilibrium flow phenomena may be analyzed. Based on the substantiation of Eqs. (3) and (5), analytical representations of the two-phase-flowfield properties allow for the evaluation of two "loss" mechanisms of interest: nozzle wall friction and interphase drag.

It will be shown that optimal contouring based on wall shear minimization is derived as a function of nozzle length scale. In addition, the essence of the interphase dynamics analysis is to optimize the nozzle length scale in a tradeoff between wall friction and phase slip. Inasmuch as the optimal nozzle contour (combined with the IHE pressure-area relationship) is used to provide the bulk flow pressure distribution for the particle dynamics analysis, there is a coupling between the following contouring and length scale estimations. Therefore, although the contouring (via wall shear minimization considerations) and length optimization (via exit bulk velocity maximization—including wall shear, interphase drag, and pressure effects) of the nozzle are carried out separately, they are not independent and the final optimal configuration reflects the integrated effect of all phenomena.

### Contouring

In order to establish a nozzle contour which "encourages" the IHE flowfield, an optimization procedure was developed in which the wall friction, integrated over the nozzle surface area, is minimized. This procedure may be compared to the approach in Ref. 2 wherein a specific family of nozzle pressure profiles is selected a priori. The particular profile which provides the maximum exit bulk velocity is assumed to be optimal. These approaches are also to be contrasted with classical wave cancellation contouring of gas flow nozzles.

Applying traditional variational principles to the integral  $\int \omega^2 C_1 dS$ , the following equation for the cross-sectional area distribution of nozzles (whose shape remains similar throughout) may be derived

$$\begin{aligned} \bar{A} \ddot{\bar{A}} - \dot{\bar{A}}^2 / 2 = & \frac{gh}{1+2gh} \left\{ \frac{d_h f}{d_h \bar{A}} \right\} \bar{A} \\ & + \left( \frac{g}{g-1} \right) \frac{(h+1) - gh}{1+2gh} \left\{ \frac{d_h f}{d_h \bar{A}} \right\} \bar{A}^2 \end{aligned} \quad (6)$$

where

$$f = \beta \bar{u}^2 \bar{A}^h, \quad g = (1 + \bar{c}^2) / \bar{A}, \quad h = \delta U(\bar{A}) \bar{A}$$

and

$$e = (dL/D_0)^{-2}, \quad \delta = cE/(L/\bar{u}^2), \quad l = (d\beta/d\bar{A}) / (\beta \bar{u}^2) \quad (7)$$

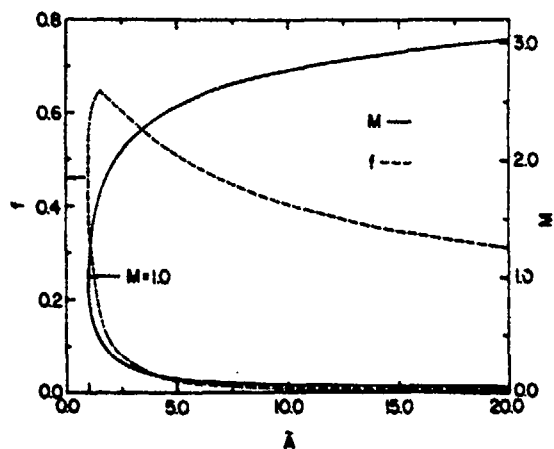


Fig. 1  $f$  and  $M$  vs  $\bar{A}$ .

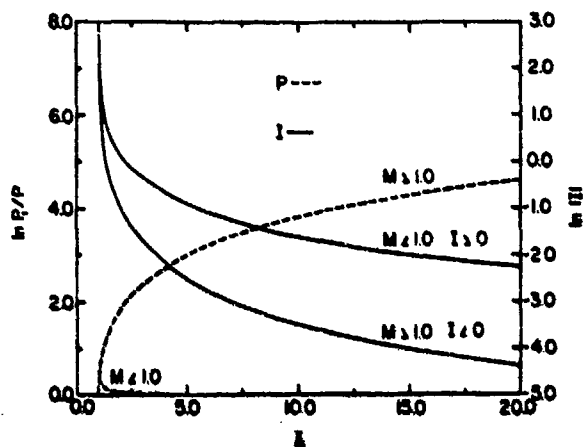


Fig. 2  $\ln(p_1/p)$  and  $\ln(1/l)$  vs  $\bar{A}$ .

In order to derive Eq. (6), the Euler-Lagrange equation:

$$\frac{d}{d\bar{A}} \frac{\delta J}{\delta \dot{\bar{A}}} - \frac{\delta J}{\delta \bar{A}} = 0 \quad (8)$$

which expresses the minimum value for a definite integral  $\int J(\bar{A}, \dot{\bar{A}}, \bar{A}) d\bar{A}$ , is applied to  $\int \omega^2 C_1 dS$ . In this case,  $J = f g^h (1+h)$  where  $f$  includes the dynamic pressure and local body radius effect,  $g$  accounts for the change in local wetted area due to the angle of the nozzle surface, and  $h$  accounts for changes in  $C_1$  due to pressure gradients. Note that Eqs. (1-5) allow  $f$  and  $l$  to be expressed as functions of  $\bar{A}$  and Eqs. (7) convert  $J$  to a function of  $\bar{A}$  and  $\dot{\bar{A}}$  with  $e$  and  $\delta$  as parameters in the optimization. These characterize the nozzle aspect ratio and sensitivity of wall friction to pressure gradient, respectively.

Figure 1 presents both subsonic and supersonic branches of  $f$  and  $M$  as a function of area ratio, with the maximum value of  $f$  occurring at  $\bar{A} = 1.65$  and  $M = 1.79$ . The corresponding results for  $l$  and  $p_1/p$  are presented in Fig. 2. Given an optimal pressure distribution,<sup>2</sup> the nozzle contour is, therefore, known. However, in this research, the optimal area distribution (for a given length scale) shall be inferred from the solution of Eq. (6) and the resultant implied pressure gradient used to optimize the length scale based on subsequent phase slip considerations.

### Phase Dynamics

The IHE limit model and associated optimal nozzle area distribution allow the particle/gas dynamics to be approached

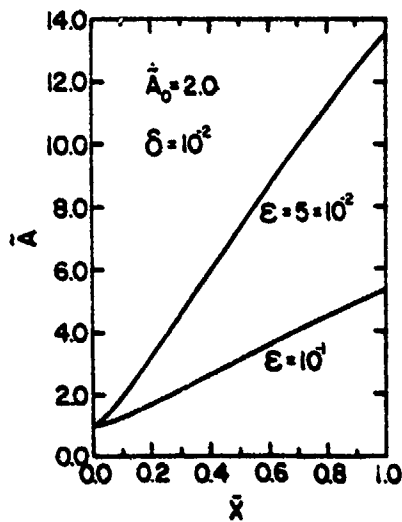


Fig. 3  $\bar{A}$  vs  $\bar{x}$  for  $\bar{A}_0 = 2.0$ ,  $\delta = 10^{-2}$ , and  $\epsilon = 5 \times 10^{-2}, 10^{-1}$ .

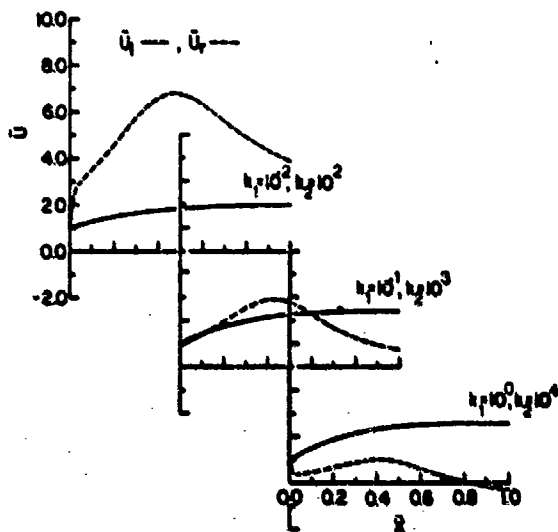


Fig. 4  $\bar{u}$ , and  $\bar{u}$ , vs  $\bar{x}$  for various  $k_1$  and  $k_2$ .

in a particularly convenient way, in order to complete the optimization procedure. Under the assumption of high  $v_1$ , the IHE pressure-area relationship and optimal area distribution are input to the analysis to provide pressure and area as a function of  $\bar{x}$  for a given nozzle length scale (aspect ratio). In this case, the phase slip and liquid velocities are computed from<sup>1,4</sup>

$$\frac{d\bar{u}_1}{d\bar{x}} + \frac{k_1}{D_H} \bar{u}_1 = \mp k_2 (1+r) \lambda_1 \lambda_2 \beta \frac{\bar{u}_1^2}{\bar{u}_1}$$

$$-\frac{k_1 \lambda_1}{D_H} \bar{u}_1 - \frac{\lambda_1 d\beta/d\bar{x}}{\lambda_2 \beta (\bar{u}_1 + \lambda_1 \bar{u}_1)}$$

$$\bar{u}_1 \frac{d\bar{u}_1}{d\bar{x}} = -\lambda_1 d\beta/d\bar{x} \pm k_2 \lambda_2 \beta \bar{u}_1^2 \quad (9)$$

These equations are also dependent upon the various length scales of the problem. Therefore, some iteration with the optimum area distribution is required.

### Results

At this point, validation of the approach relies primarily on the data in Ref. 2, wherein two different air/water nozzles

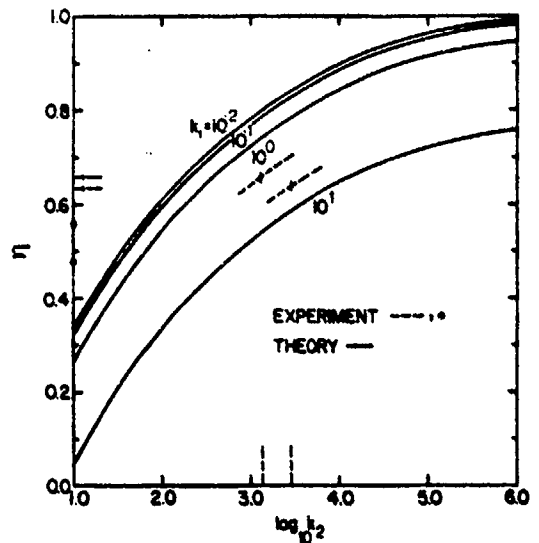


Fig. 5  $u$  vs  $k_2$  for various  $k_1$ , compared to the experimental data of Ref. 1.

were analyzed and tested at  $(p_1/p_2) = 35$  with  $r = 10$ . These nozzles had identical subsonic contraction cones and two different length supersonic sections (7 vs 21 deg divergence angles), with the same overall area ratio. Therefore, the area contour and length optimization developed here will also focus on the supersonic regime. This avoids complex particle breakup dynamics modeling, inasmuch as liquid particulates typically reach a limiting size at the throat.<sup>1,2</sup>

Given a reliable particle breakup model (e.g.,  $W_e = W_e(\frac{r}{r_1})$ ), the entire nozzle may be computed with the same contour and particle dynamics analysis (utilizing the local particle scale), inasmuch as the IHE pressure-area relationship is applicable to the entire nozzle. For cases of fixed-size particles, the entire nozzle may be computed utilizing these equations without modification.

Typical integration of Eq. (6) from the throat to the exit plane is presented in Fig. 3 and indicates that a simple (nearly) linear area distribution is often optimal. (For axisymmetric nozzles, this results in a configuration approaching a bell shape.) The similarity between these shapes and those in Ref. 2 is remarkable. This, combined with the substantiation of Eqs. (3) and (5) indicates that the information provided in Ref. 2 on the effect of nozzle length should also be relevant to the length scaling optimization procedure developed here.

Note that the solution to Eq. (6) is a split-point boundary value problem.  $\bar{A}_0 = 1$  is required by definition of  $\bar{A}$  and the origin of integration at the throat. Either the subsonic or supersonic nozzle regions may be evaluated, depending on which branch of  $f$  and  $l$  are chosen as the integration proceeds away from the throat. For a given  $\epsilon$  and  $\delta$ , in order to obtain the desired  $\bar{A}_0$ , the appropriate  $\bar{A}_0$  is determined iteratively. In lieu of this iteration, the computations may be carried out with  $\bar{A}_0$  as a parameter. A family of nozzle shapes/area ratios is thereby developed.

For a  $(p_1/p_2) = 35$  and  $r = 10$ , the IHE pressure-area relationships are combined with the optimal contour to solve Eqs. (9) and generate profiles of liquid and slip velocities along the nozzle for various values of  $k_1$  and  $k_2$ . Typical results are shown in Fig. 4, which illustrate a dependence on nozzle length similar to that presented in Ref. 2. The negative values of  $\bar{u}$ , shown for  $k_1 = 10^0$  and  $k_2 = 10^0$  reflect a somewhat unphysical disparity between  $C_1$  and  $C_2$ , with the wall shear stress dominating.

It may be shown that the bulk (mass flow-weighted mean) velocity is related to the slip and liquid velocities by

$$\bar{u} = u_1 - r u_2 / (1+r) \quad (10)$$

The measured bulk velocities in Ref. 2 are 170 and 183 m/s for nozzles I (7 deg) and II (21 deg) and resulted in efficiencies ( $\eta$ ) of 0.48 and 0.56, respectively. Utilizing Eqs. (9) and (10), the computed nozzle efficiency is plotted in Fig. 5 as a function of  $k$ , for various  $k_2$ . Compared with the data from Ref. 2, it is seen that the trend toward higher efficiency with shorter nozzles is predicted analytically. For these flow conditions, this dependence is observed only for large  $k$ , nozzles, due here to the small throat hydraulic diameter of annular nozzles.

### Conclusion

An approximate, self-consistent procedure has been developed to determine the optimal area ratio, contour, and aspect ratio of two-phase-flow nozzles with large volume ratios. Results of the analysis have been validated by comparison with experimental data obtained from nozzles which closely approximate the computed optimal configuration. At this stage of the analysis, fixed-size particles were considered in the assessment of optimal nozzle aspect ratio. However,

given a reliable particle size model for any given situation, the identical procedure may be employed utilizing a variable particle scale.

### Acknowledgment

The author would like to acknowledge the assistance of Prof. D.W. Netzer in providing information which was crucial to the evaluation of the analytical results obtained during this research.

### References

- <sup>1</sup> Warner, C.F. and Netzer, D.W., "An Investigation of the Flow Characteristics of Two-Phase Flow in Converging-Diverging Nozzles," ASME Paper 63-WA-192, Winter Annual Meeting, Philadelphia, Pa., Nov. 1963.
- <sup>2</sup> Elliott, D.G. and Weinberg, E., "Acceleration of Liquids in Two-Phase Nozzles," NASA Tech. Rept. 32-987, July 1968.
- <sup>3</sup> Clift, R., Grace, J.R., and Weber, M.E., *Bubbles, Drops and Particles*, Academic Press, New York, 1978.
- <sup>4</sup> Wallis, G.B., *One-Dimensional Two-Phase Flow*, McGraw-Hill Book Co., New York, 1969.